國立交通大學

光電工程學系
顯示科技研究所

碩士論文

自由空間微光機電元件蝕刻孔陣列之
光學繞射分析

Optical Diffraction of Etch-Holes Array on

Free-Space Micro Optical Devices

研究生：洪健翔

指導教授：田仲豪 博士

中華民國九十五年七月

自由空間微光機電元件蝕刻孔陣列之
光學繞射分析

Optical Diffraction of Etch-holes Array on

Free-Space Micro Optical Devices

研 究 生: 洪健翔　　　　　　Student: Chien-Hsiang Hung

指導教授: 田仲豪　　　　　　Advisor: Dr. Chung-Hao Tien

國立交通大學 電機學院

光電工程學系

顯示科技研究所

碩士論文

A Thesis

Submitted to Display Institute & Photonic Department

College of Electrical Engineering Science

National Chiao-Tung University

in Partial Fulfillment of the Requirements

for the Degree of Master

In

Display Institute

July 2006

Hsin-Chu, Taiwan, Republic of China.

中華民國九十五年七月

致謝

　　首先要感謝我指導教授田仲豪老師兩年來在研究上、表達能力及生活細節上無私的細心指導，並且提供我們良好的研究環境，使我在碩士生涯對於微光學元件與微機電技術有深入的了解，並順利完成本論文。

　　實驗室的日子裡，首先要感謝李企桓學長在各方面的指導與協助，還有韋安琪、鄭璧如學姊、林洭宏、楊柏儒學長在研究過程提供許多寶貴的建議，同時還要感謝其他學長姊、同學和學弟在課業上、生活上、研究上的幫助與分享，並陪伴我一起度過兩年快樂的日子。

　　此外，我要感謝成大趙儒民教授和朱甫翊、許智超學長，在研究期間提供我實驗材料以及技術上的協助，讓我實驗得以順利進行。

　　最後，對於我的父母、哥哥、及女友，我要感謝你們多年來的支持與鼓勵，還有生活上的細心照顧與關懷，使我能夠無後顧之憂的研究與學習，並順利完成碩士學業。這份喜悅我將與幫助過我的各位分享。

自由空間微光機電元件蝕刻孔陣列之
光學繞射分析

研究生：洪健翔　　　　指導教授：田仲豪 博士

國立交通大學
光電工程學系 顯示科技研究所

摘要

　　微光機電系統中，在最後蝕刻犧牲層來使結構層懸浮的過程，一般來說會利用分部於結構層上的蝕刻孔來增加下方犧牲層的蝕刻率，而減少蝕刻劑對於結構上的過度蝕刻。然而，以一般周期性陣列分部的蝕刻孔在光學應用上會造成強烈的繞射場，高階的繞射光會造成雜訊及不預期的干擾。

　　本論文以費朗和夫繞射理論為基礎，建立了一套用來分析蝕刻孔陣列繞射之模型，並分析及討論在不同蝕刻孔分布下的繞射效應，期望藉由設計不同之蝕刻孔陣列來改變出光場型而減少不必要的繞射光束，甚至以蝕刻孔陣列達到系統需求的出射光場。最後利用自動組裝的面型微加工技術製作出微反射面鏡來驗證光學特性是否符合計算結果，量測結果與理論預期的相當接近，期望此提出之蝕刻孔排列設計在微光機電面型微加工的設計規則上可提供有用的改進。

Optical Diffraction of Etch-holes Array on Free-Space Micro Optical Devices

Student: Chien-Hsiang Hung   **Advisor: Dr. Chung-Hao Tien**

Department of Photonics & Display Institute
National Chiao Tung University

Abstract

Optical micromachining or micro-electro-mechanical systems (MEMS) typically require etch holes to reduce the time required to release the micromechanical structure during the sacrificial undercutting. However, high-order diffraction beams caused by the periodic etch-holes array often deteriorate the optical performance by generating noise and erroneous crosstalk signals in most optical systems.

In this thesis, a model based on Fraunhofer diffraction theory is presented to study the dependence of diffraction behavior on various etch-holes array. The microreflectors are produced by self-assembly surface micromachining technology to verify the simulation. Comparison with experimental results confirms the validity of this model. The proposed design of random distributed etch-holes array is expected to provide a useful consideration for future surface micromachining design rule.

Table of Contents

Figure Caption

Table Caption

Chapter 1

Introduction

1.1 Surface Micromachining in Optical MEMS

Microoptics have expanded widely over the last decade in terms of their diverse applications in device and instrumentation. For most applications, integration of discrete optical components into a fully function system is crucial, in order to reduce size and cost, as well as to enhance the robustness and stability. The micromachining, or microelectromechanical systems (MEMS) technology can implement a functional system to be monolithically integrated on a single chip via a VLSI-like process (VLSI: very large scaled integrated), thus provides a potential route to meet such requirements. In addition, mechanical components such as hinged and rotating structures combined with a compact microactuator allow a moveable function in operating. This advantage can perform more complex function and has been widely applied in many optical systems such as optical display, data storage, switches, and sensors. Fig. 1.1 (a), (b), (c) show the applications on display, and they are digital micromirror device (DMD) chip, raster-scanning display system, and the grating light valve (GLV) display, respectively [1]-[3]. Fig. 1.1 (d) shows the micro pickup applied in storage as the other potential application [4].

Among various MEMS fabrication technologies, surface micromachining process, with the polysilicon thin film grown by low pressure chemical vapor deposition (LPCVD) as the structural layer and the silicon dioxide thin film as the sacrificial material, are the most popular approach for its integrated circuit (IC)-like foundry process.[5]-[6]

(a)

(b)

(c)

Moving Ribbon

Fixed Ribbon

Air Gap

Silicon Substrate

MEMS Micro-Optical Bench

(d)
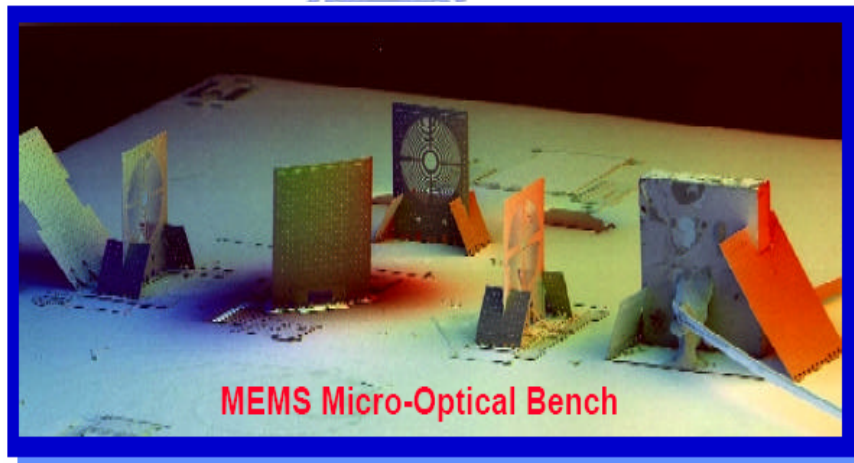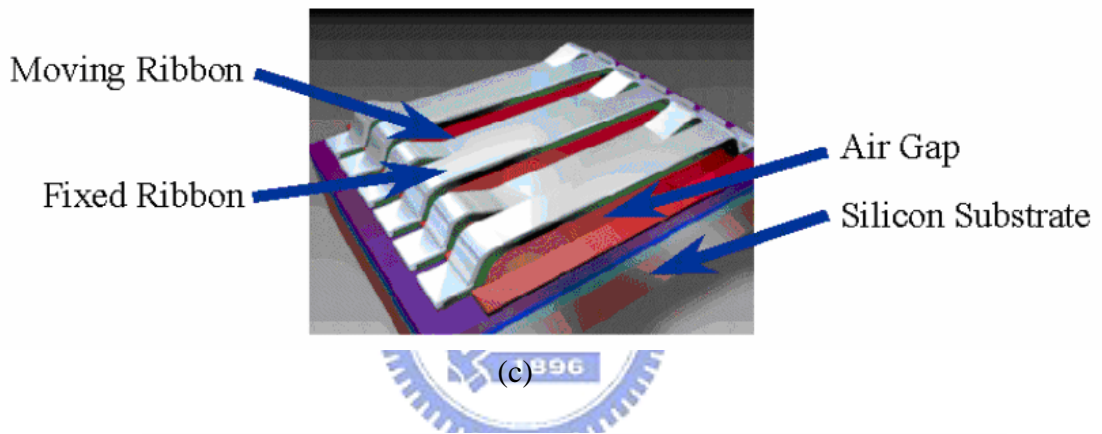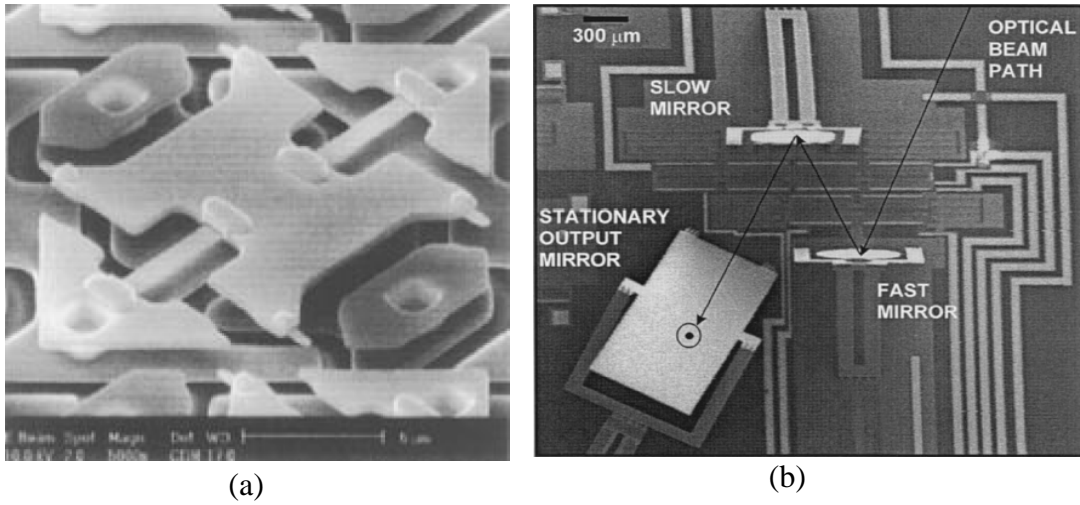
Fig. 1.1 The applications of (a) DMD chip developed at Texas Instruments, (b) raster-scanning display system developed by P. M. Hagelin et al, (c) the grating light valve developed by D.M. Bloom, and (d) micro pickup developed by M. C. Wu et al.

1.2 Etching Holes in MUMPs Process

For surface micromachining technology, the most well known recipe is the Multi-User MEMS Process (MUMPs) [7], has been used for the purpose of fast and lost-cost development. In MUMPs, devices have been fabricated using polysilicon thin film grown by low pressure chemical vapor deposition (LPCVD) as the structural material and silicon oxide as the sacrificial material due to the excellent mechanical properties of polysilicon and high selectivity of sacrificial etching with hydrofluoric acid. A critical MEMS-specific fabrication step required to release microstructures is the selective removal of the sacrificial layer.

The sacrificial layer etch is at the heart of a MEMS micromachining process, it is typically desirable to minimize its duration so that all undesirable etching of other films or structures is reduced. To facilitate the release of a large-area microstructure such as microreflector, thin film micro beam splitter, or polysilicon-based optical devices, so-called etching holes are typically formed in the microstructure. Without any etching holes, the etchant used to remove the sacrificial layer must slowly undercut the large-area structure, resulting in long release etch time. The use of etching holes allows the etchant to immediately access even the center of the large-area microstructure and increases the undercutting rate. The result is that the time required to release a large-area microstructure is no longer a function of its area, but rather only the density of etching holes. One example of a free-space optical beam splitter is shown in Fig. 1.2, where etching holes are periodically spaced in a two-dimensional array. These etching holes are inevitable for such free-space plate-type devices.
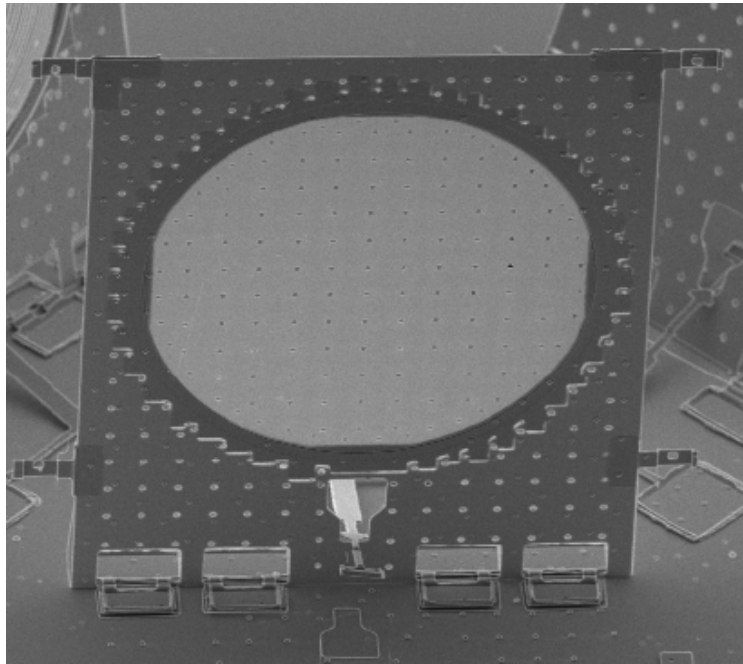
Fig 1.2 The micro BS with etch-holes array.

1.3 Optical Properties of Devices with Etching Holes

The effects of the etch-holes array on the electromechanical and ferromagnetic properties have been discussed before [8]-[9]. However, only a few papers have been dedicated to the behavior of diffraction, and they mainly reported this topic numerically and lack an analytical consideration [10]. Excluding the scatter caused by roughness, the absorption by material, and other physic effects, the diffraction from a perforated thin film with a square etch-holes array is described, which is the most typical mask layout in the surface micromachining process. Fig. 1.3 shows the field distribution diffracted from a device with square etch-holes array, where the high order diffracted beam will cause undesirable noise and crosstalk signal.
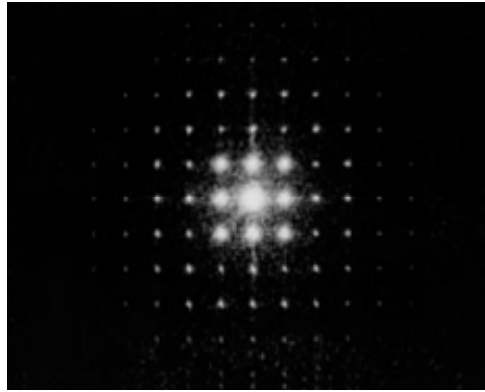
Fig 1.3 The field distribution diffracted by a square etch-holes array.

1.4 Motivation and Objective of this Thesis

In this thesis, the diffraction from a perforated thin film with a square etch-holes array is first described. To reduce such high order beams of the output is a consequential goal. We propose applying various distributed etch-holes layouts to modulate the incident beam for different output. The objective is to modulate the light for what we expect via etch-holes array and to provide a useful consideration for future surface micromachining design rule. Two types of array layout will be introduced. One is random distributed array to reduce the high order diffraction beam; the other is circular distributed array to shape the incident beam.

1.5 Organization of this Thesis

This thesis is organized as following: The principle of diffraction theory is presented in Chapter 2. In Chapter 3, the calculation and the results of the etch-holes array are presented. The processes to fabricate a microreflector which is developed to verify the calculated results are described in Chapter 4. The experimental results and the discussion will be shown in Chapter 5. Finally, the summary of this thesis and future works will be presented in Chapter 6.

Chapter 2

Principle

2.1 Huygens-Fresnel Principle [11]

The Huygens-Fresnel principle describes that every point on the primary wavefront is considered as a source of secondary spherical wavelets, with the same frequency and velocity as the primary wave. The amplitude of the field at any point is the superposition of all these wavelets, taking account of their amplitudes and phases, that is, the amplitudes and phases of secondary wavelets could interfere with each other. The principle is illustrated in Fig. 2.1.
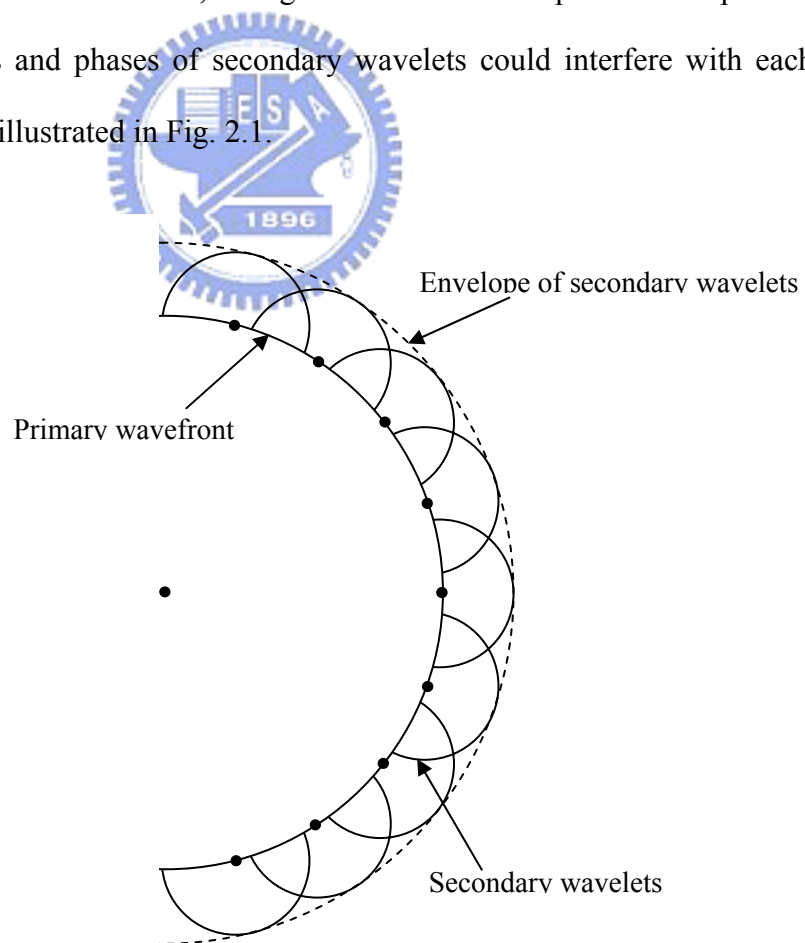
Fig. 2.1 Hygens' wavefront construction

2.2 Scalar Diffraction Theory

Maxwell's equation is the beginning for our analysis. Assume that there are no sources present in a dielectric medium which is linear, homogeneous, and isotropic. The equations are written as

$$\nabla \times \vec{E} = -\mu \frac{\partial \vec{H}}{\partial t} \tag{2.1}$$

$$\nabla \times \vec{H} = \varepsilon \frac{\partial \vec{E}}{\partial t} \tag{2.2}$$

$$\nabla \cdot \varepsilon \vec{E} = 0 \tag{2.3}$$

$$\nabla \cdot \mu \vec{H} = 0 \tag{2.4}$$

where ε is the permittivity and μ is the permeability of the medium. The vector identity is

$$\nabla \times \left(\nabla \times \vec{E} \right) = \nabla \left(\nabla \cdot \vec{E} \right) - \nabla^2 \vec{E}. \tag{2.5}$$

Substituting the Maxwell's equations for E and H, into (2.5), we can obtain two equations,

$$\nabla^2 \vec{E} - \frac{n^2}{c^2} \frac{\partial^2 \vec{E}}{\partial t^2} = 0 \tag{2.6}$$

$$\nabla^2 \vec{H} - \frac{n^2}{c^2} \frac{\partial^2 \vec{H}}{\partial t^2} = 0 \tag{2.7}$$

where n is the refractive index of the medium, defined as $n=(\varepsilon/\varepsilon_0)^{1/2}$, and ε_0 is the vacuum permittivity. The symbol c mean the velocity of propagation in vacuum.
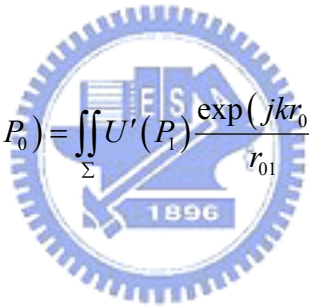
The components of the electric and magnetic field behave identically and can be described by a single scalar wave equation,

$$\nabla^2 u(x,y,z,t) - \frac{n^2}{c^2} \frac{\partial^2 u(x,y,z,t)}{\partial t^2} = 0 \tag{2.8}$$

where $u(x, y, z, t)$ represents any of the scalar field components, and t is a time variable. Assuming a time-harmonic steady-state solution in which the partial time derivative can be replaced by $j\omega$, the Helmholtz equation can be yield as

$$\left(\nabla^2 + k^2\right)U = 0 \tag{2.9}$$

here $U= u(x, y, z, t)$, and k is the wave number, given by $k = \dfrac{2\pi}{\lambda} = \dfrac{n\omega}{c}$, where ω is the angular frequency , and λ is the wavelength in the dielectric medium. From Green's theorem and under some assumptions and derivations, we can obtain the Fresnel-Kirchhoff diffraction formula,

$$U(P_0) = \iint_{\Sigma} U'(P_1) \frac{\exp(jkr_{01})}{r_{01}} ds \tag{2.10}$$

Where

$$U'(P_1) = \frac{1}{j\lambda} \left[\frac{A\exp(jkr_{21})}{r_{21}} \right] \left[\frac{\cos(\vec{n}, \vec{r}_{01}) - \cos(\vec{n}, \vec{r}_{21})}{2} \right]. \tag{2.11}$$

$U'(P_1)$ represents the secondary sources with its amplitudes and phases. It can be explain as the spherical wave illuminating from a point source located at P_2 to the point P_1 on the aperture and weighted its own related obliquity factor, which describes a contribution of angle relation to $U(P_0)$. The relationship in space shows in Fig. 2.2, where Σ means the size of the aperture.
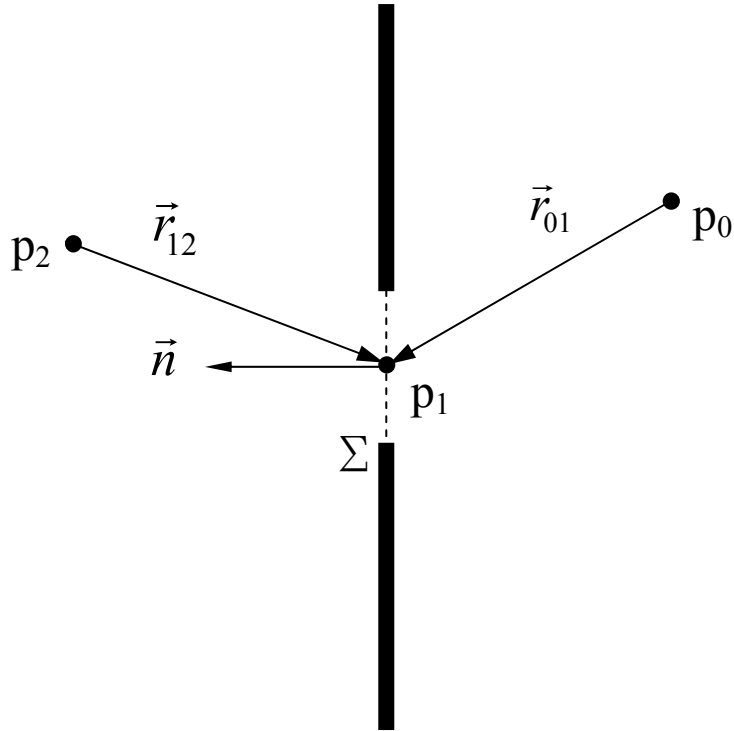
Fig. 2.2 Point-source illumination of a plane aperture

In general case, r_{01} and r_{21} are extremely greater than the size of the aperture, so we assume the obliquity factor $[\cos(\vec{n}, \vec{r}_{01}) - \cos(\vec{n}, \vec{r}_{21})]/2$ will be roughly constant, ~1. The Fresnel-Kirchhoff diffraction formula can be rewritten as

$$U(P_0) = \frac{1}{j\lambda} \iint_{\Sigma} U(P_1) \frac{\exp(jkr_{01})}{r_{01}} ds \qquad (2.12)$$

where $U(P_1)$ means a spherical wave on the aperture diverging from a point source at P_2, and is defined as $U(P_1) = \left[A\exp(jkr_{21})/r_{21} \right]$. It express the observed field $U(P_0)$ as a superposition of diverging spherical wave $\exp(jkr_{01})/r_{01}$ originating from secondary sources located at each and every point P_1 within the aperture Σ.

2.3 Fresnel and Fraunhofer Diffraction

2.3.1 Fresnel Diffraction

Before introducing a series of approximations to the scalar diffraction theory, it will be in more explicit form for the case of rectangular coordinates. Fig. 2.3 shows the relation of the object plane and the observed plane on rectangular coordinates in space. According to Eq. (2.12), we can rewrite it as

$$U(x,y) = \frac{1}{j\lambda} \iint\limits_{\Sigma} U(s,t) \frac{\exp(jkr_{01})}{r_{01}} ds\,dt. \qquad (2.13)$$
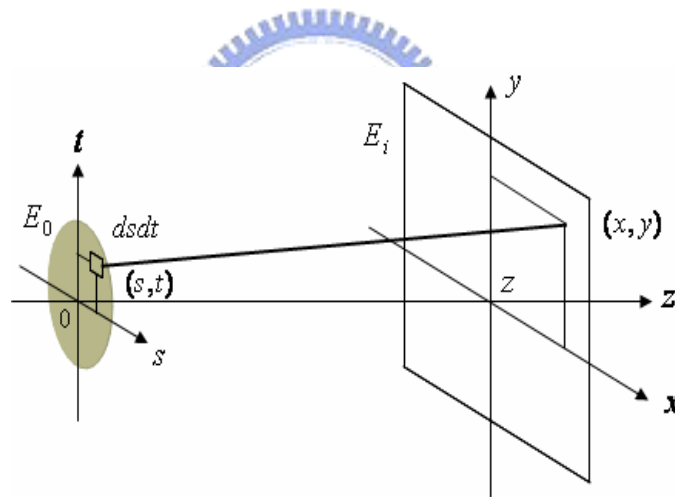
Fig. 2.3 Relation of the scale diffraction theory

By some approximation, the r_{01} can be replaced by

$$\vec{r}_{01} = \sqrt{z^2 + (x-s)^2 + (y-t)^2}$$
$$\approx z\left[1 + \frac{1}{2}\left(\frac{x-s}{z}\right)^2 + \frac{1}{2}\left(\frac{y-t}{z}\right)^2\right]. \qquad (2.14)$$

The resulting expression for the field at *(x,y)* therefore becomes

$$U(x,y) = \frac{e^{jkz}}{j\lambda z}\iint_{\infty} U(s,t)\exp\left\{j\frac{k}{2z}\left[(x-s)^2+(y-t)^2\right]\right\}dsdt. \qquad (2.15)$$

Eq. (2.16) is readily seen to be a convolution, and expressed in the more clear form

$$\iint_{\infty} U(s,t)h(x-s,y-t)dsdt \qquad (2.16)$$

where *h* can be seen as the impulse response in the optical system, and defined as

$$h(x,y) = \frac{e^{jkz}}{jkz}\exp\left[\frac{jk}{2z}(x^2+y^2)\right]. \qquad (2.17)$$

In fact, *h*(x,y) provide a parabolic phase weight. We can explain Eq. (2.16) that the diffraction field *U*(x,y) is the field *U*(s,t) taken convolution with a parabolic pahse exponential, the impulse response of a free space system. Moreover, the other form of Eq. (2.16) is found:

$$U(x,y) = \frac{e^{jkz}}{j\lambda z}e^{j\frac{k}{2z}(x^2+y^2)}\iint_{\infty}\left\{U(s,t)e^{j\frac{k}{2z}(s^2+t^2)}\right\}e^{-j\frac{2\pi}{\lambda z}(xs+yt)}\,dsdt, \qquad (2.18)$$

which we recognize to be the Fourier transform of the product of the complex field just to the right of the aperture and a parabolic phase exponential.

11

2.3.2 Fraunhofer Diffraction

Referring to Eq. (2.16) and (2.19) as the Fresnel diffraction formula, which is valid in the near field of the object plane. For the far field diffraction, the condition will be met if the distance z satisfies

$$z \gg \frac{k\left(s^2+t^2\right)_{\max}}{2}. \tag{2.19}$$

Eq. (2.19) can be further simplified as

$$U\left(x,y\right)=\frac{e^{jkz}}{j\lambda z}e^{j\frac{k}{2z}\left(x^2+y^2\right)}\iint_{\infty}U\left(s,t\right)e^{-j\frac{2\pi}{\lambda z}\left(xs+yt\right)}\,dsdt, \tag{2.20}$$

which is well known as the Fraunhofer diffraction formula. It relates the diffraction field to the object field by Fourier transform. We note that Fourier transform remains valid for Fresnel and Fraunhofer diffraction. It means that we can calculate the diffracted fields in the fraunhofer region with accuracy of the Fresnel approximation. Fig. 2.4 shows the relation of the two approximations along the optical axis with the different distances from an aperture.
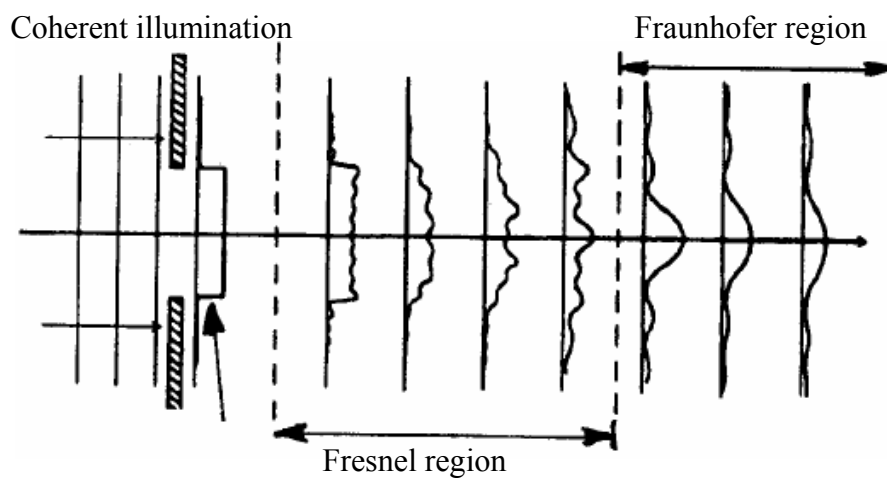
Fig. 2.4 The relation of the two approximations along the optical axis

2.4 Analysis of Etch-holes Array with Babinet's Principle [12]

The Babinet's principle can be used to analyzing the diffraction of the etch-holes array on MEMS devices. We can assume the field outputted from a mirror as a 2-dimension grating with periodic. This reflected field is the same with a transmitted field. It is more convenience for us to create the model for different kinds of devices, either reflection type or transmission type.

From the Fresnel-Kirchhoff diffraction formula, the Babinet's principle can be developed. Two masks like those of Fig. 2.5, in which clear and opaque regions are simply reversed, are called complementary apertures. If one of the mask, say A, and then the other, B, are put into place and the amplitude at some point of the screen is determined for each, the sum of these amplitudes must equal the unobstructed amplitude there. The diffracted fields of A and B can be expressed as

$$E_A + E_B = E_u,$$ (2.20)

with A and B representing any two complementary apertures. An interesting special case of Babinet's principle is a point where E_u=0. Then, by Eq. (2.22),

$$E_A = -E_B$$ (2.20)

and

$$I_A = I_B$$ (2.21)

at the point.
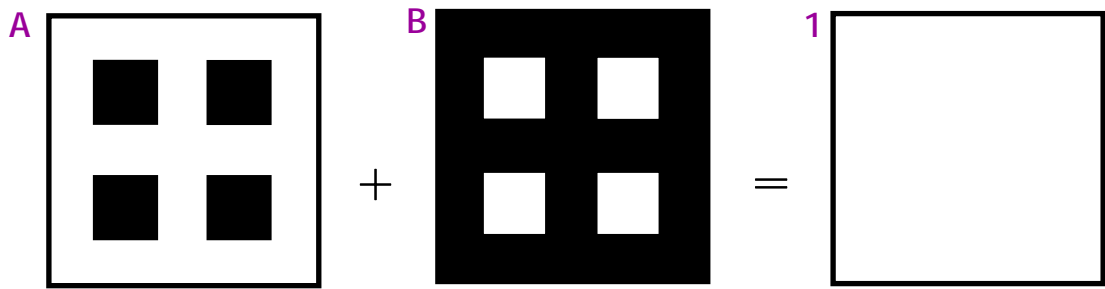
Fig. 2.5 Two complementary aperture

In practice, Fresnel diffraction dose not produce amplitudes Eu=0 without an aperture. Fraunhofer diffraction does in the case of the pattern formed by a point source and a lens. For the region outside the small Airy disc, Eu is zero, essentially. Thus positive and negative transparencies of the same pattern produce the same diffraction pattern in Fraunhofer diffraction.
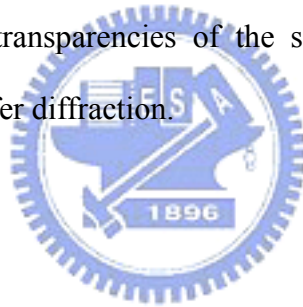
Chapter 3

Simulation

3.1 Introduction

As we described in Section 1.2, the etch holes are inevitable for free- space features under surface micromachining technologies. Chapter 3 describes the analysis of diffraction from etch-holes array. The array with regular spacing, the standard case in MEMS design rule, will be discussed first. Moreover, the random distribution and circular distribution are then proposed for different purposes.

In the typical design, the sizes of each elements (d) and the distances between the holes (s) should be kept in a range of *d= 2~5μm* and *s= 20~30μm*, respectively Smaller size of etch holes will cause the etchant can't immediately permeate the sacrificial layer under the microstructures. Longer distances between the holes will cause incomplete release, whereas closer distances will cause the film to crack easily. We can arrange different layouts from the traditional case in these design rules.

3.2 Diffraction from Etch-holes Array with Regular Spacing

The diffraction caused by a two-dimensional (2D) etch-holes array is analogous to the case in which a uniform plane wave is diffracted by a crossed grating. In this case, the features on the perforated film are treated as scalar amplitude objects. This means that the incident beam is simply modulated by a complex transmission (or reflection) coefficient introduced by the properties of microstructure with etch- holes array. Here we ignore the physics of interaction between the etch hole and the

incident beam in the conformity with the relief pattern and assume aperture part merely imports to the incident beam an amplitude modulation. Despite the fact that solving the Maxwell equation is most exact way for diffraction analysis, approximating etch holes as amplitude objects holds well for our case where typical aperture sizes of MEMS structure are much larger than the working wavelength. In addition, we can avoid entailed massive computations and get a fast calculation. The wavelength λ for the simulation is 633 nm. However, as long as two conditions are met (1) the diffracting etch hole must large compared with wavelength, and (2) the diffracting fields must not be observed too close to the aperture [11], the calculated values can be applied to different wavelengths by scaling all the geometry parameters involved proportionally. Fig. 3.1 illustrates the transmission function $B(x,y)$ of a perforated die and geometric parameters for diffraction calculation. If the overall size of the die is limited to $c \times n$, etch holes have a size of $a \times l$ and are spaced b and m apart in the x and y directions, respectively, then the transmission function of the etch-holes array can be expressed as

$$B(x,y) = \left[rect(\frac{x}{a}) \otimes comb(\frac{x}{b}) \right] rect(\frac{x}{c}) \times \left[rect(\frac{y}{l}) \otimes comb(\frac{y}{m}) \right] rect(\frac{x}{n}), \quad (3.1)$$

where $rect(x/a)$ is a rectangular function of width a. The function for such an aperture is defined as

$$rect(\frac{x}{a}) = \begin{cases} 1 & |x| \le \dfrac{a}{2} \\ 0 & |x| \le \dfrac{a}{2} \end{cases}, \quad (3.2)$$

and the comb function is defined as

$$comb(\frac{x}{b}) = b \sum_{k=-\infty}^{\infty} \delta(x-kb) \quad (3.3)$$

Note that etch-holes array with regular spacing can be generated by convolving the rectangular function *rect(x)* with *comb(x)*.
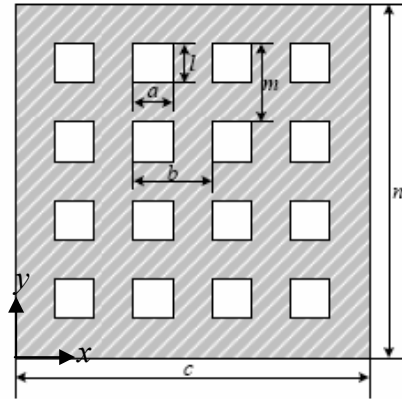
Fig. 3.1 The transmission function *B(x,y)*

For a typical MEMS device where propagation distance *z* is much larger compared with *x'* and *y'* (the axes on image plane), the diffraction by 2D etch- holes array can be estimated using Fraunhofer diffraction formula, by which the diffracted pattern is obtained as the Fourier transform of the transmission function, that is *F{B(x)}= E(fx, fy)*, where the argument *fx = sin θx/ λ ≈ x'/ λz* and *fy = sin θy/ λ ≈ y'/ λz*, as shown in Fig. 3.2. The Fourier transform of the comb function is

$$F\left\{comb(x,b)\right\} = b \sum_{k=-\infty}^{\infty} comb(f_x, \frac{1}{b}). \tag{3.4}$$
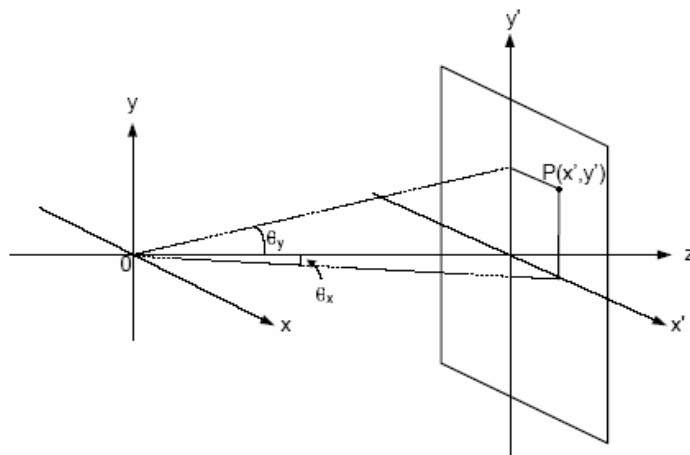
Fig. 3.2 Geometric parameters of diffraction calculation

Consequently, we can obtain the amplitude distribution of the wave diffracted through the perforated film

$$E(f_x, f_y) = F\{B(x,y)\}$$

$$= F\left\{ \left[rect(\frac{x}{a}) \otimes comb(\frac{x}{b}) \right] rect(\frac{x}{c}) \times \left[rect(\frac{x}{l}) \otimes comb(\frac{x}{m}) \right] rect(\frac{x}{n}) \right\}$$

$$= asinc(af_x)\left[csinc(cf_x) \otimes comb(f_x, \frac{1}{b}) \right] lsinc(lf_x)\left[nsinc(nf_x) \otimes comb(f_x, \frac{1}{m}) \right]$$

$$= asinc(af_x)\left[\frac{c}{b}sinc(cf_x) \otimes \sum_{k_x=-\infty}^{\infty} \delta(f_x - \frac{k_x}{b}) \right] lsinc(lf_x)\left[\frac{n}{m}sinc(nf_x) \otimes \sum_{k_y=-\infty}^{\infty} \delta(f_x - \frac{k_x}{b}) \right]$$

$$= alsinc(af_x)sinc(lf_x)\left[\sum_{k_x=-\infty}^{\infty} \sum_{k_y=-\infty}^{\infty} N_x N_y sinc(c(f_x - \frac{k_x}{b})) \times sinc(n(f_y - \frac{k_y}{m})) \right]$$

$$(3.5)$$

where N_x and N_y are the number of etch holes in the x and y directions, respectively. Fig. 3.3 shows the irradiance distribution of a square etch-holes array with $a = l = 5\mu m$, $b = m = 20\ \mu m$ and $c = n = 200\ \mu m$. Because the order of the dimension in the transmission pattern is $a < b < c$, the order of the diffracted pattern which is the Fourier transform of the etch- holes array has an inverse relationship; namely,

$$\frac{1}{c} < \frac{1}{b} < \frac{1}{a} \tag{3.6}$$

where $1/c$ is the size of an individual spot, $1/b$ is the spacing between each spikes, and $1/a$ is the overall size of the diffraction pattern [13]. When the ratio of the aperture width a and the period b is an integer, the minimum of the envelope will exactly coincide with some of the spikes of the array pattern. In this case, $b/a = 4$, the fourth spikes overlaps with the first null of side lobe and the intensity of the fourth spike thus disappears. Since the intensity distribution is obtained as

$$I(f_x, f_y) = E^*(f_x, f_y) \cdot E(f_x, f_y) \tag{3.7}$$

accordingly, we can calculate the intensity

$$I = I_0 sinc^2(af_x)sinc^2(lf_y)\left[\sum_{k_x=-\infty}^{\infty}\sum_{k_y=-\infty}^{\infty} sinc^2(c(f_x - \frac{k_x}{b}))sinc^2(n(f_y - \frac{k_y}{m}))\right]$$

$$= I_0 sinc^2(af_x)sinc^2(lf_y)\left[\frac{sin(\pi cf_x)}{N_x sin(\pi bf_x)}\right]^2\left[\frac{sin(\pi nf_y)}{N_y sin(\pi mf_y)}\right]^2 \qquad (3.8)$$

which can be verified through the serial expansion

$$\frac{1}{sin\,x} = \sum_{k=-\infty}^{\infty}\frac{(-1)^k}{x - \pi k}. \qquad (3.9)$$
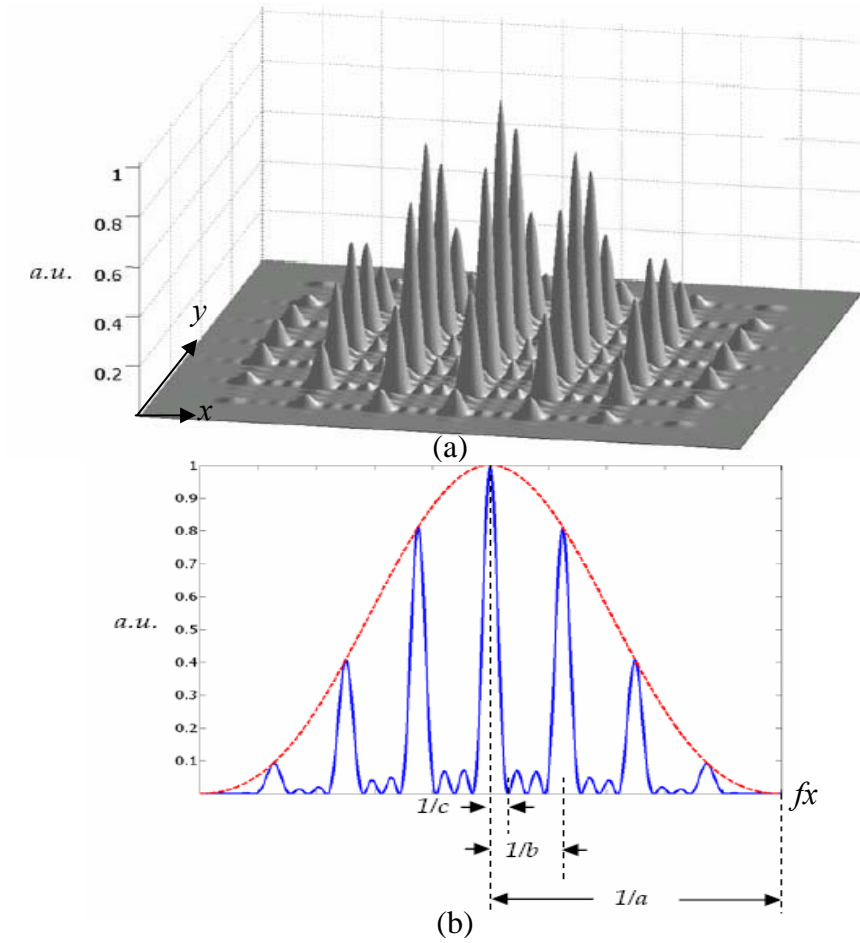

(a)

(b)

Fig. 3.3 (a) The membrane perforated by a square etch-holes array,
(b) irradiance cross-section, where the order of the pattern
has an inverse relationship of the etch-holes layout.

19

It can be seen from Eq. (3.8) that the diffracted pattern is contributed by two factors of different natures. The factors outside the square brackets are determined solely by the shape of aperture element and are called the shape factor, which appears as the envelope of the diffraction pattern. On the other hand, the factors inside the square brackets are determined solely by the period and die size of etch- holes array, are called the array factor. The diffracted pattern is the product of these two factors.

Sometimes the actual shape of etch holes after plasma etching tends to be circular rather than square due to imperfect photolithography and etching process. In this case, *sinc* function caused by the rectangular element in Eq. (3.5) can be substituted by the *Bessel* function, which is the Fourier transform of the circular aperture. Similarly, when the surface area of a microstructure is relatively larger than the illuminated spot size, the overall size is determined by the spot size rather than the external border of the device. Therefore, *sinc* function caused by the rectangular die should be replaced by the *Bessel* function as well.
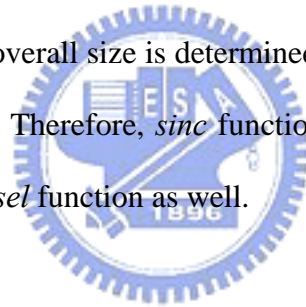
3.3 Diffraction from Etch-holes Array with Random Distribution

According to the preceding study, we note that periodicity of the etch- holes array leads to considerable amount of high- order beams. In the above case, the normalized intensity of the lowest few orders are 1 [0th order], 0.8113[(1,0), (0,1) order], 0.6582 [(1,1) order], 0.4072 [(2,0), (0,2) order]. Such high- order diffraction beams are often undesirable to the optical performance by generating noise and erroneous crosstalk signals in most optical systems. Let us examine an etch- holes layout, where etch holes are randomly arranged but without any rotation of the individual elements, as shown in Fig. 3 4 (a), where the dash lines represent the original position of each etch hole and solid lines represent the random offset from the

original one. For simplicity, we ignore the external border and only consider one- dimensional case. If each square Aperture is translated in the x direction by a random distance b_k from its original position, then the transmission function can be represented by

$$B(x) = \sum_{k=0}^{N_x-1} rect(\frac{x - b_k}{a}) \qquad (3.10)$$

where the translated distance b_k are generated by the computer according to discrete uniform distribution [14]. Using the shift property of the Fourier transform,

$$F\{h(x \pm b_k)\} = e^{\mp j2\pi f_x b_k} H(f_x). \qquad (3.11)$$

The amplitude distribution in far field can be expressed by

$$E(f_x) = sinc(af_x)\left[1 + e^{-j2\pi b_1 f_x} + e^{-j2\pi b_2 f_x} + e^{-j2\pi b_3 f_x} + \ldots\ldots\right]. \qquad (3.12)$$

Therefore

$$I = E^*E = sinc^2(af_x)\left(N_x + 2\sum_{j=1}^{N_x-1}\sum_{k=1}^{N_x-1} \cos 2f_x(b_j - b_k)\right), \qquad (3.13)$$

since b_j and b_k are random in this case, the translation corresponds to a superposition of cosine functions with a random period, which leads the interference term in Eq. (16) to zero. Such analysis can be extended to 2D case and the intensity of the diffracted wave thus becomes $N_x N_y sinc^2(af_x)sinc^2(lf_x)$, as shown in Fig. 3.4 (b), where the grid pattern due to the array factor is average out and the diffraction pattern is solely determined by the form factor of each element but with N times the intensity.
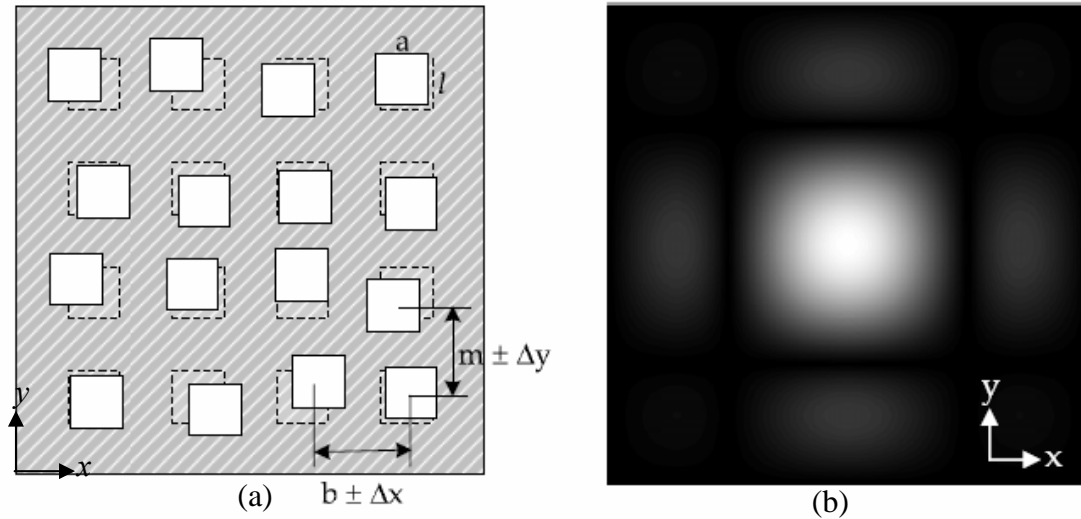
Fig. 3.4 (a) Geometric parameters of the translated etch-holes layout, dash lines represent the original position and solid lines represent the random offset by discrete uniform distribution, and its (b) calculated irradiance.

Although random spacing is an effective approach to eliminate the high- order diffracted beams and thus alleviate the crosstalk effect, one more requirement should be noted when failure mechanisms are taken into consideration [15]. Because typical surface micromachining uses polysilicon thin film as the structure layer and the silicon oxide thin film as the sacrificial layer. If the spacing of etch holes on the polysilicon layer is too far, the etchant is hard to access the center of the large- area micromechanical structure, thereby failing to release the component. On the contrary, while the spacing is too close, the stress concentration is accumulated around the etch holes and the polysilicon film is easily cracked during the fabrication or assembly process. Therefore, one more condition is needed that the spacing between each etch hole b_k should be limited in the range of 20±5 μm in this case. We can further randomize each aperture element with respect to rotation angle θ as well as translation, as shown in Fig. 3.5 (a). Since the form factor of etch holes has been randomized with center symmetry, the calculated irradiance in Fig. 3.5 (b) looks like one obtained by rotating the diffracted field of a single square aperture about it's center.
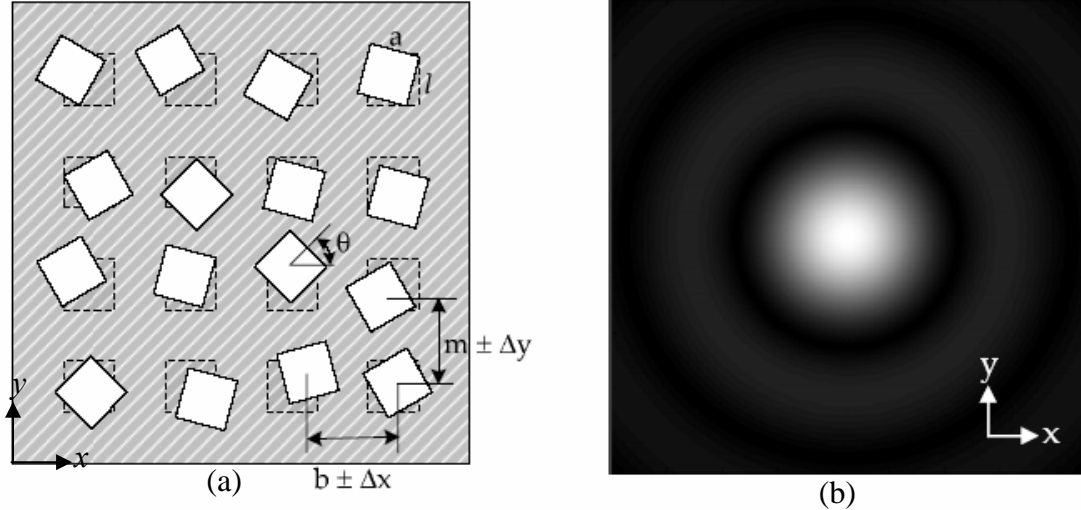
Fig. 3.5 (a) Geometric parameters of the translated etch-holes layout, dash lines represent the original position and solid lines represent the position after random translation and rotation, and its (b) calculated irradiance.

3.4 Diffraction from etch holes array with concentric layout
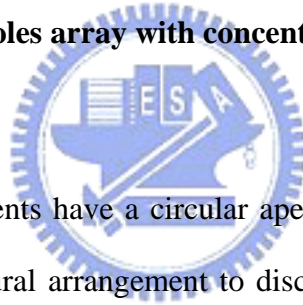
Since most optical elements have a circular aperture, compare with rectangular grid pattern, it is a more natural arrangement to discretize a circular boundary by a grid of concentric circles shown in Fig. 3.6. To fit the geometric symmetry, here we design circular holes, and let the rectangular grid be replaced by a family of concentric circles with radius r_m given by

$$r_m = md \qquad m = 0,1,2,\ldots, \tag{3.14}$$

with d the spacing. If we design the same spacing d between adjacent elements along any circle, then

$$2\pi r_m = 2m\pi d = N_m d \tag{3.15}$$

In which N_m is the number of elements on the m-th ring. It is clear that the values of N_m that satisfy Eq. (3.15) are not integers, but one can round the results to the nearest integer. Taking the typical case, $R = 333\mu m$ and $d = 40\mu m$, for example, there are 4 concentric circles, and the numbers of etching holes per ring are given in Table-3.1, under the restriction that N_m be divided by 6, so that there exists a quadratic symmetry. Here the factor θ_m means the angle of the sector which separate one element from the other one corresponding to the origin on m-th ring, and it is clear that θ_m is different magnitude for different m. This gives 61 elements in the array, exactly the same density as were used in the rectangular grid array. Therefore, the circular grid pattern would not cause any difficulty in the consideration of wet etching process.

Table 3.1 the geometric parameters of each ring on the concentric array

m	0	1	2	3	4
$N_m = 2\pi r_m/d$	1	6	12	18	24
$\theta_m = 2\pi/N_m$	0	60	30	20	15

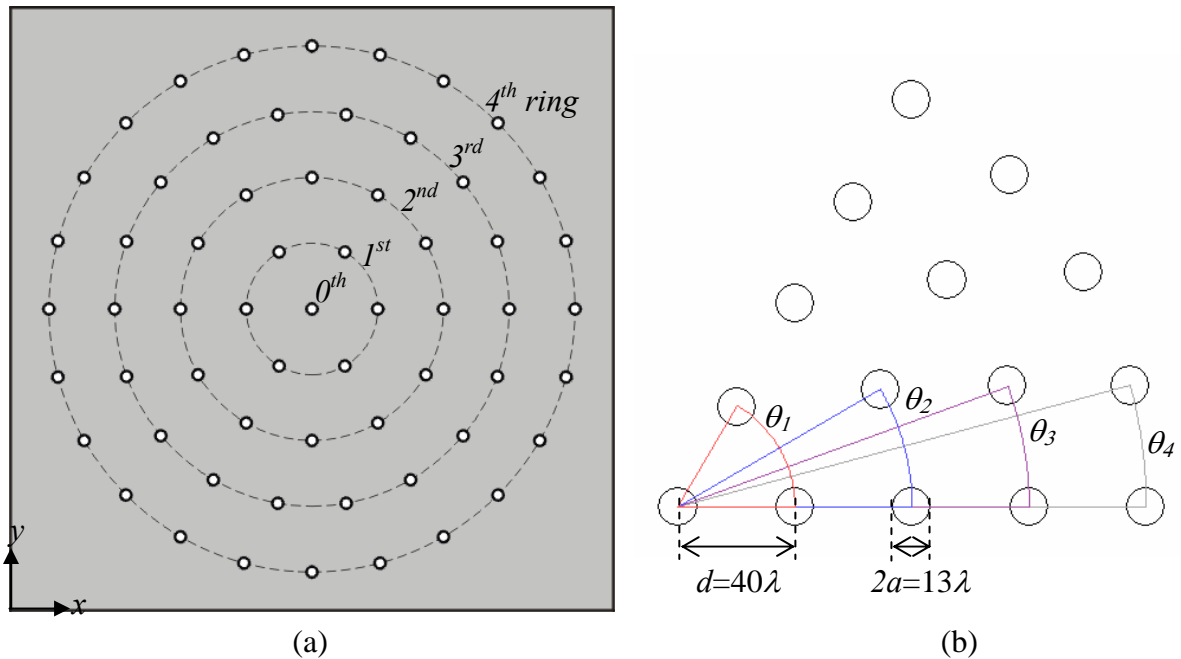(a)   (b)

Fig. 3.6 (a) The concentric array, (b) 1/6 circle of the layout with its geometric parameters

To describe the diffraction patterns of the circular multiaperture systems, a geometric analysis was performed for the concentric rings of identical circular etching holes. The transmittance $t(r)$ can be written as the convolution ($\otimes$) of the transmittance of the unit circular element $circ(r/a)$ with an array of delta functions $\delta(r)$, which describe the position of each etching holes.

$$t(r) = circ\left(\frac{r}{a}\right) \otimes \left[\sum_{m=0}^{M} \sum_{n=0}^{N_m} \delta(r - md, \theta - n\theta_m)\right], \qquad (3.16)$$

where a is the radius of each subapertures, and M is the maximum ring numbers within a given pupil size. The diffraction pattern can be analyzed from the transmittance function illuminated by a normally incident laser beam. Based on Fraunhofer diffraction theory, the analysis is consisted of examining the far-field diffraction patterns produced by imaging a point source through multiaperture system. The following expression is used to calculate the diffraction patterns propagating a distance z

$$h(f_s, f_t) = \frac{a}{\rho} J_1(2\pi a \rho) \times \sum_{m=0}^{M} \sum_{n=0}^{N_m} \exp\left[-j2\pi r_m (f_s \cos n\theta_m + f_t \sin n\theta_m)\right]. \quad (3.17)$$

This is the impulse response, where (s, t) represents the scaled coordinates in the image plane, and (f_s, f_t) are their spatial frequency. The symbol ρ represent the radial spatial frequency and can be replaced by $(f_s^2 + f_t^2)^{1/2}$. Excluding nonessential proportionality factors, it is proportional to the Fourier transform of the transmittance of the exit pupil, which is formed by the combination of each exponential component

with a 1st Bessel function as the envelope. We can also get its intensity distribution from $I=h*h$. Fig. 3.7 illustrates the relation of the symbols between the object plane and the image plane in free space.
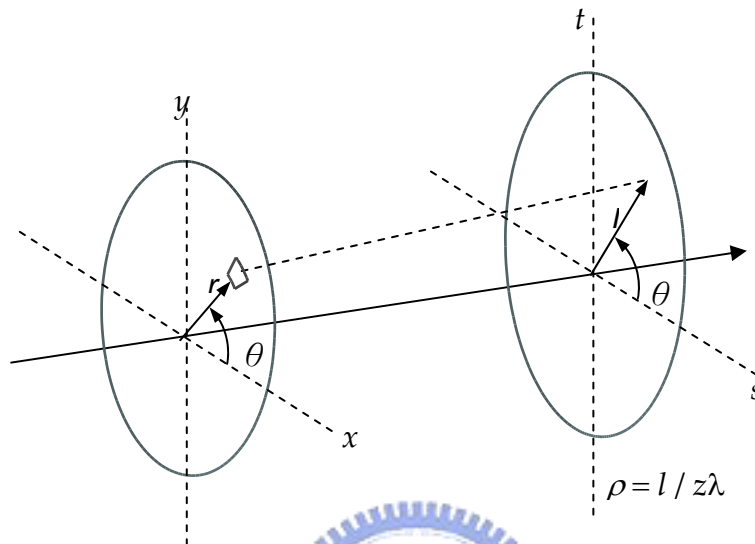

Fig. 3.7 The relationship between the object plane and the
image plane in free space in the polar coordinates

The purpose of this study was to design a circular etching holes layout with transmission (or reflectance) that exhibit the central beam widths and side picks irradiances less than that of the conventional rectangular arrangement. The amplitude function can be expanded as the superposition of the diffraction patterns caused by each concentric circle grids. It is noted that the complex field amplitudes generated by each ring is determined by the argument of each exponential.

The normalized irradiance distribution of this symmetric circular array we calculated is shown in Fig. 3.8. It is seen to consist of a main beam additional to a family of side picks. In order to quantify the results, we define the diffraction efficiency as $E = I_{\max} / I_0$, where I_0 and I_{max} are the intensity of the central main beam and the high order beam with the maximum magnitude, respectively. From the results, the diffraction efficiency is about 50%. To reduce the intensity of the side picks, we

expect it cause destructive interference between the fields created by each concentric ring. Without varying the arrangement density and the well-etching interval between holes, we choose to rotate the m-th ring of the layout with half of the separated angle, $\theta_m/2$, respectively. Fig. 3.9 shows the finally calculated distribution. When only 4th ring is rotated with the angle $\theta_4/2$, the most pulses around the central beam will be destructive interference by each shifted Bessel function on 4th ring. In this case, the diffraction efficiency E is reduced to 18%.
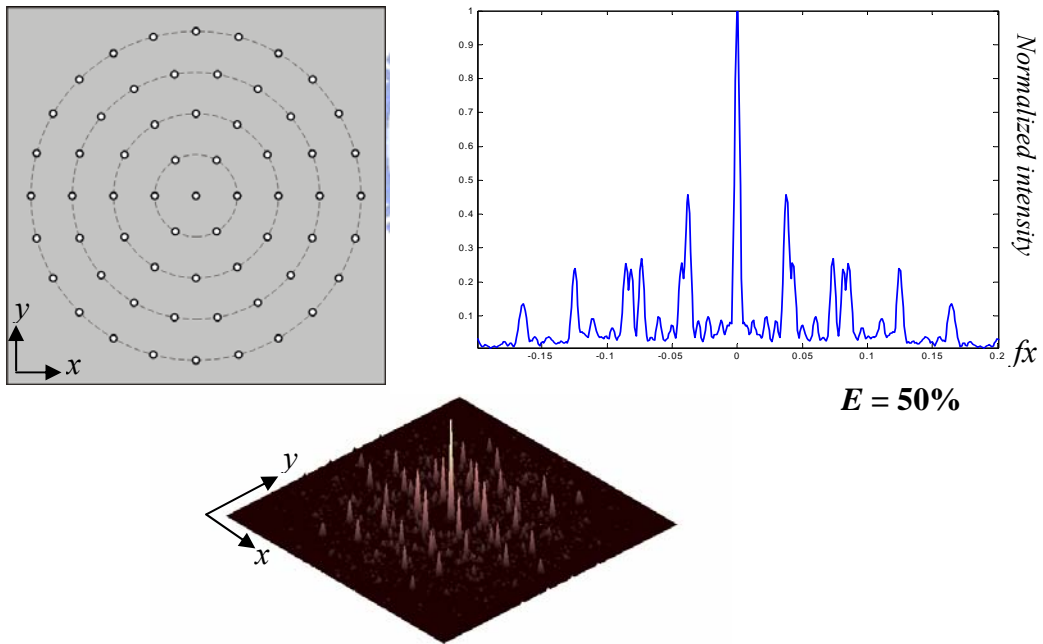
Fig. 3.8 the symmetric circular layout with the
diffraction irradiance and its lateral view
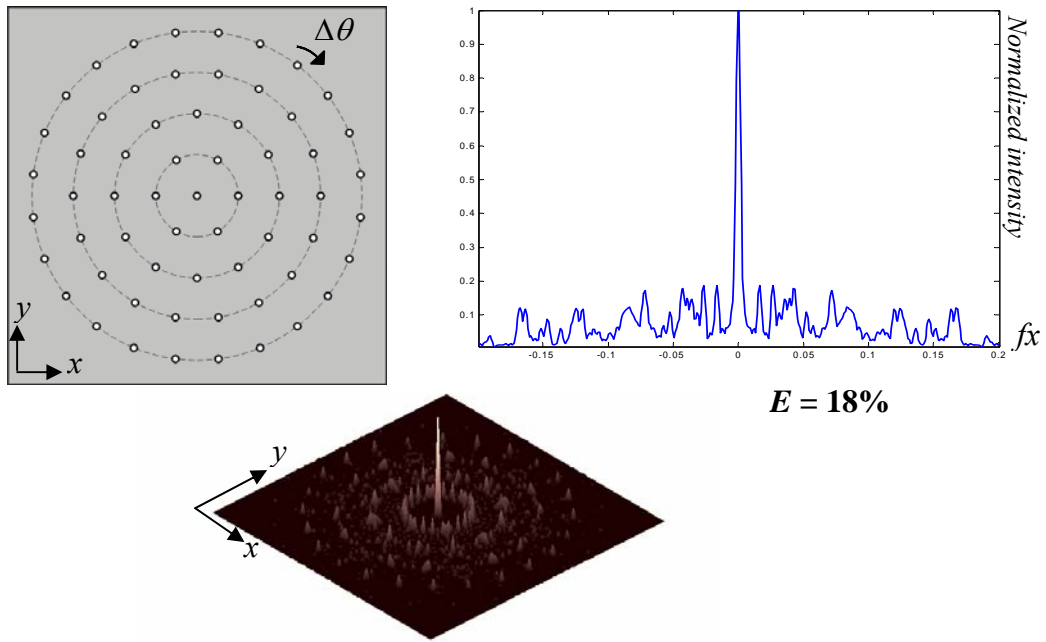
Fig. 3.9 the circular layout with $\theta_4/2$-rotated 4th
ring and the diffraction irradiance

Fig. 3.10 shows the lateral view. Where the dot line, the dash line, and the solid line express the diffraction patterns caused by the regular array, the concentric array, and the concentric array with rotated ring, respectively. Comparing their diffraction efficiency, we can find the regular case has the highest magnitude. The diffraction efficiency can be reduced to 18%~50% by destructive interference.
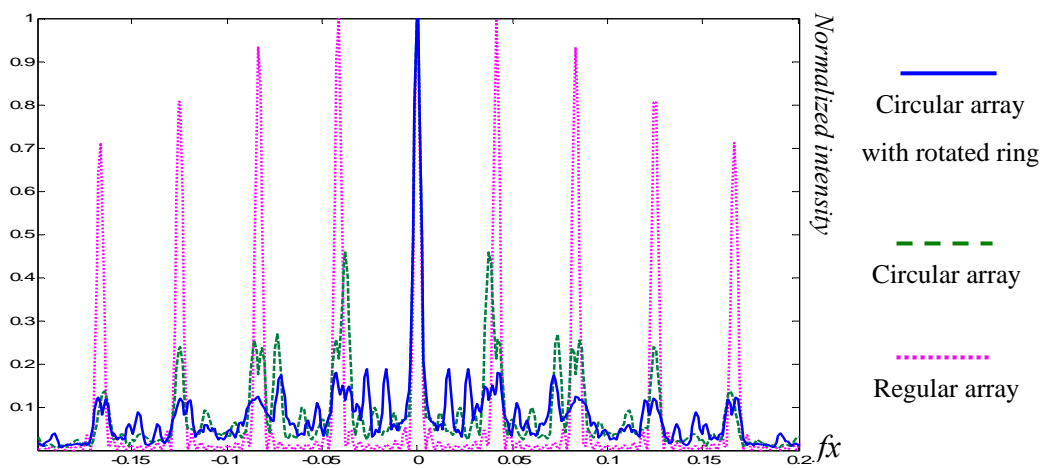
Fig. 3.10 the lateral views of circular cases
compared with regular array.

3.5 Summary

Based the fraunhofer theory, the diffraction patterns caused by etch-holes array are calculated, and we design the distribution for the purpose to improve the optical properties. The traditional case has many high order diffraction beams and the diffraction efficiency at least 80%. First, the random distribution can causes an uniform beam. Besides, we used the concentric array to make the high order beams destructive interference, and the diffraction efficiency are successfully reduced to 18%~50%.

Chapter 4

Fabrication

4.1 Introduction

To verify the analysis, we produce the microreflectors with the designed etch-holes layouts. A microreflector is uncomplicated to produce, and is the most fundamental device in all three-dimensional micro-opto-mechanical systems (MOEMS). Fig. 4.1 shows a microreflector produced by Syms. et al [15].
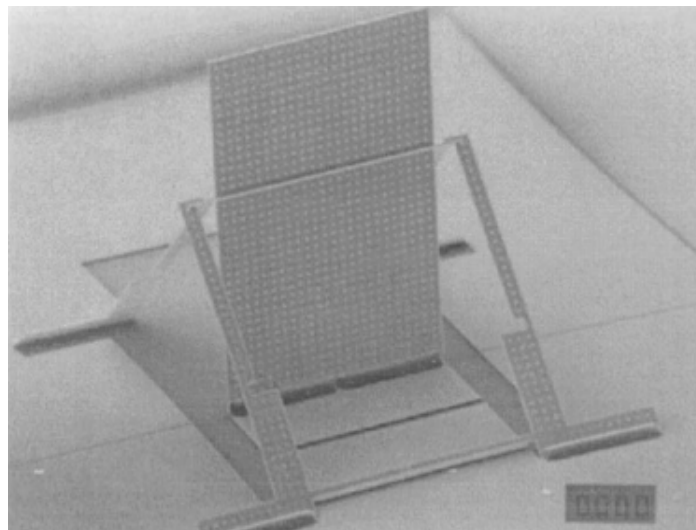
Fig. 4.1 A pop-up microreflector used this self-assembly process.

The pop-up microreflector was generally fabricated based on a two-layer poly-silicon surface micromachining process, based on deep reactive ion etching (DRIE) of bonded silicon-on-insulator material, sacrificial etching. By designing of the anchors in MUMPs for bonded structural layers and the removed sacrificial layers, the micro-hinges are created and realize movable structure in micron scale. However, the pop-up devices assembled with the micro-hinges are still too complicated for fast

manufacture, because of 6~7-mask processes and a manual step of assembly. In recent years, R. R. A. Syms. et al. developed the process for self-assembly of MOEMS. We purpose to follow the advanced process to demonstrate the diffraction analysis in MOEMS. The device in Fig. 4.1 is a pop-up microreflector used this self-assembly process.

4.2 Photoresist-reflowing Hinge

The process of the pop-up devices developed by R. R. A. Syms. et al. is based on out-of plane rotation powered by the surface tension of thick photoresist pads. In surface tension self-assembly, small pads of a meltable material are used to link the edges of a fixed and movable parts, which are both initially coplanar. Before melting, the pads have a rectangular cross-section, and after melting, a semi-cylindrical section. By considering either the forces acting or the energy of the free liquid surface, it is possible to show the existence of a torque that tends to rotate the movable part out-of-plane. Fig. 4.2 shows the layout of the relation between fixed land, moving part and the hinge driver. The meltable material of the hinge driver should be exactly patterned, and can prevent etching by etchant, hydrofluoric acid. In before literatures, positive photoresist AZ4562 and negative photoresist BCB are both used for the hinge driver. Fig. 4.3 shows the SEM picture of the reflowing hinge using the photoresist BCB.

The advanced process provide the improvements in structure definition and design, which have led to an increase in process yield to a approximately 75% and in the best assembly accuracy to the alignment errors below 0.1. These advances greatly enhance the prospects for self-assembled MOEMS, and provide a simple way for us to demonstrate the microreflector.
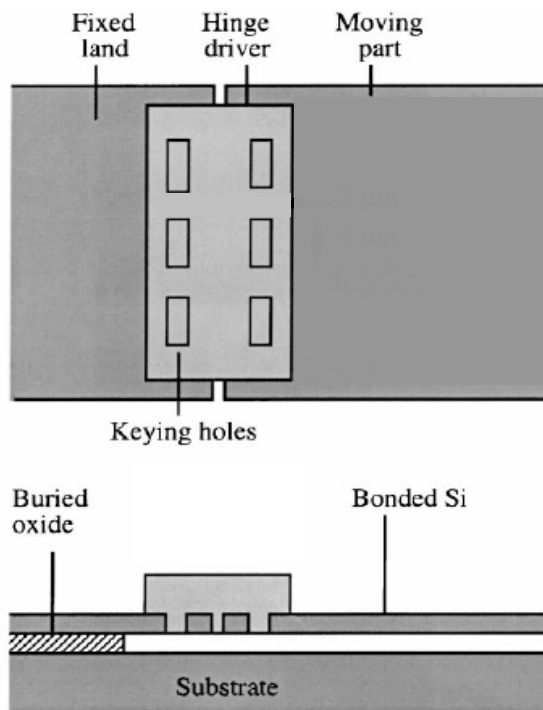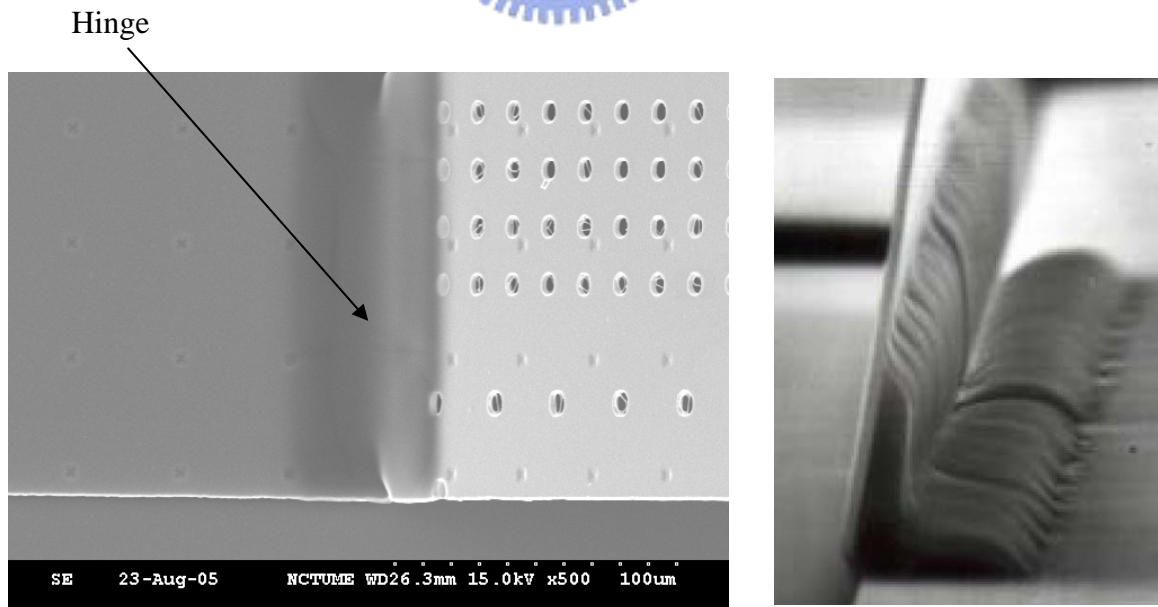
Fig. 4.2 Layout of improved hinge structure.

Fig. 4.3 SEM photographs of PR-hinges.

4.4 Fabrication

The MOEMS are best developed on bonded silicon-on-insulator (BSOI) wafers with MUMPs, because it allows the construction of thick, high quality suspended mechanical part in single crystal material. However, the BSOI wafers are high-cost materials, and more important for movable component, such as actuators, comb driver, or etc. In our case, we just want to produce a fixed device with designed etch-holes array. What we care about are the optical properties of the etch-holes array, so the MUMPs-like is used for the fabrication. The MUMPs-like we used include the $2\mu m$-thickness polysilicon for structure deposited by LPCVD under $2 \mu m$ -thickness SiO2 as the sacrificial layer deposited by PECVD. It effectively lower the cost, and is practicable to analyze the optical properties.

Our fabrication process is based on 4 inches Si (1 0 0) substrate. First, the SiO_2 with 2 μm thickness is deposited by PECVD as the sacrificial layer. Then, the dimples on the SiO_2 are etched by RIE, which can form the nail-like sticks on the under surface of poly-Si. The release process is caused by hydrofluoric acid etching SiO_2, and the interaction produce water as the residuum in the narrow space between the structures and the substrate. The surface tension of water is comparatively large in the micron scale world, so there is the striction problem preventing the movable part out-of-plane. These nail-like sticks caused by the dimples can prop up the structures from the substrate after releasing and reduce the striction problem.

After etching the dimples, the poly-Si with 2 μm thickness is deposited by LPCVD as the structural layer over the sacrificial layer. Because the poly-Si layers are quite thin, the gradient stress may cause the sheet-type structure curved after assembly. To reduce the gradient stress on the poly-Si layer, annealing for several hours of the chips is needful. Then, the etch-holes layouts and the outlines of the

structures are defined on the poly-Si layer and etched by RIE. After the structures are created, the photoresist used for the hinge driver is coated and defined as a pad linking the edges of fixed and movable parts. Finally, the chips are immersed in hydrofluoric acid to remove the sacrificial layer, SiO$_2$, and heated on the hot plate until the photoresist melt to pull up the device. Fig. 4.4 (a)-(f) expresses the whole fabrication process.

4.4 Design & Mask Layouts

Fig. 4.5 (a) shows the whole mask layouts of a 45°-fixed microreflector. After depositing the SiO2 layer on substrate, the first mask, Dimple, shown in Fig. 4.5 (b) defines the holes with regular array. Continuously, the poly-Si layer is deposited on the SiO2. The second mask, Poly, shown in Fig. 4.5 (c) defines the etch holes array and the outline of the structure. From the Poly mask, we can see the device is fixed on 45° by two arms and the etch-holes array which could be the layout we designed before. Finally, the mask, Hinge, shown in Fig. 4.5 (d) defines the photoresist as the hinge driver. In this case, to express more clearly, we assume the hinge pads are only used for positive photoresist.
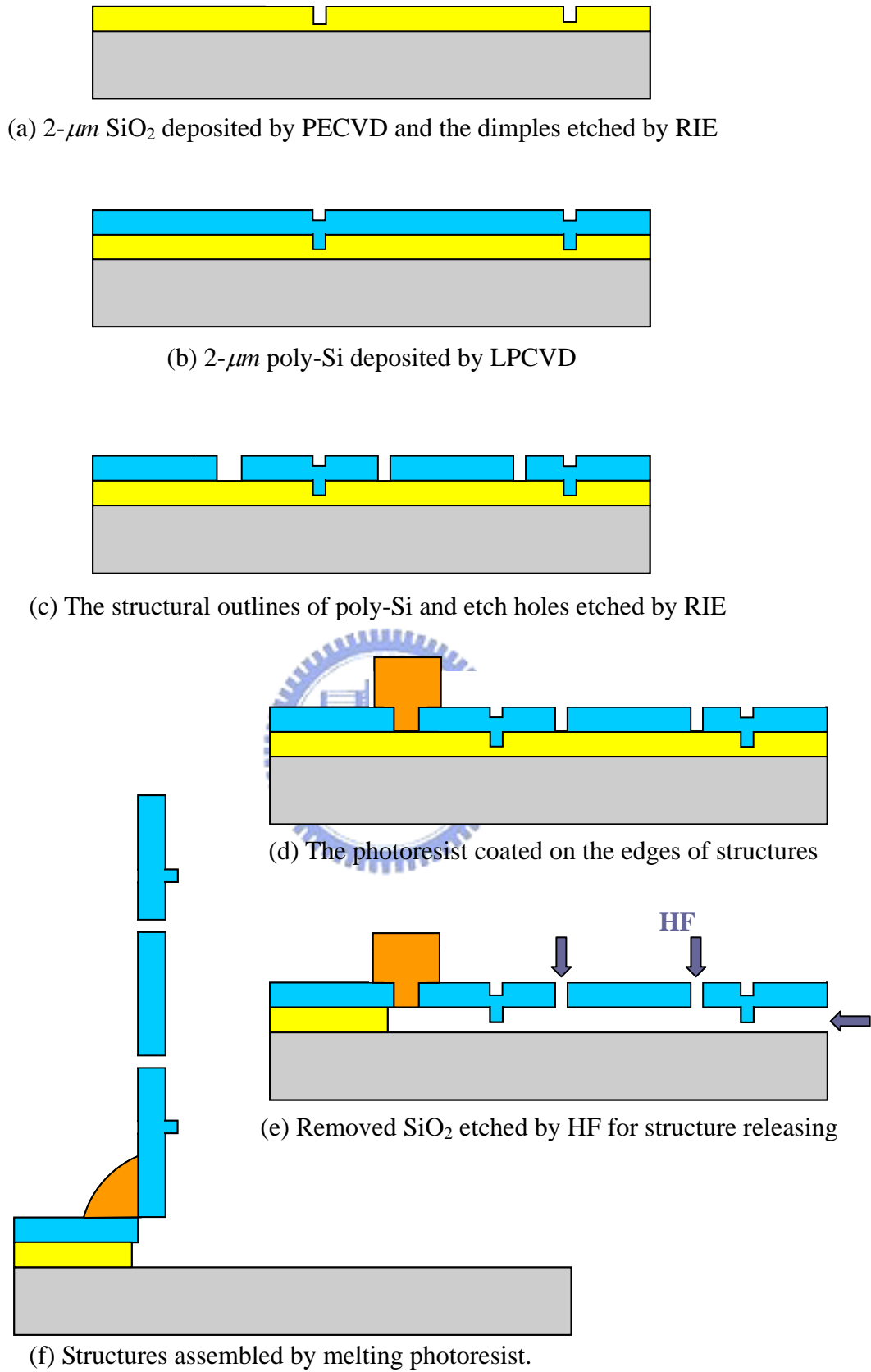
(a) 2-μm SiO$_2$ deposited by PECVD and the dimples etched by RIE

(b) 2-μm poly-Si deposited by LPCVD

(c) The structural outlines of poly-Si and etch holes etched by RIE

(d) The photoresist coated on the edges of structures

HF

(e) Removed SiO$_2$ etched by HF for structure releasing

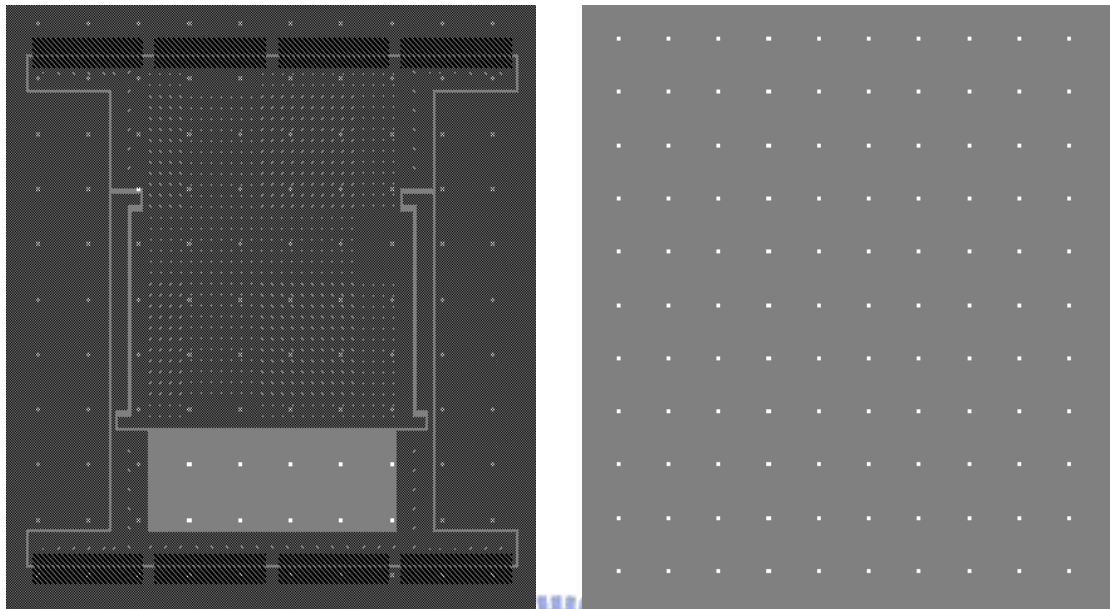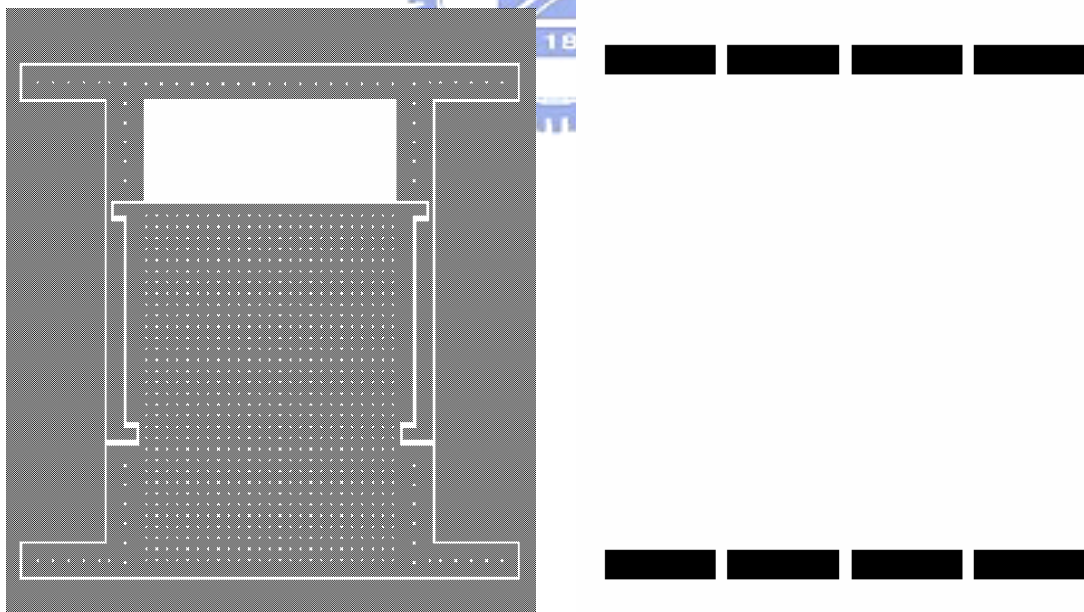(f) Structures assembled by melting photoresist.

Fig. 4.4 (a)-(f) The flow of fabricating a micromirror.

(a) The whole layout

(b) Dimple

(c) Poly

(d) Hinge

Fig. 4.5 (a)-(d) Mask layouts

4.5 Summary

To analyze the optical properties with etch-holes array, the simply microreflectors are qualified. If the reflectivity of poly-Si is not high enough to measure, we can coat aluminum over the devices after all the processes. However, the reflectivity, transmissivity, surface roughness, or other factors which effect optical properties can be neglected in this thesis. The 45°-fixed microreflector is demonstrated, and the 90°-fixed micro polarization beam splitter (PBS) with Si_3N_4 thin film is further developed by this advanced process.

Chapter 5

Experimental Results

5.1 Introduction

According to the simulation and fabrication presented in the previous chapters, the experimental results will be shown in this chapter. The measurement system used to evaluate the irradiance distributions will be described first. Then the fabricated pop-up devices will be shown. After that, the measurement of the diffraction fields will be performed to make sure if the fabricated etch-holes array match the design goal.

5.2 Measurement System
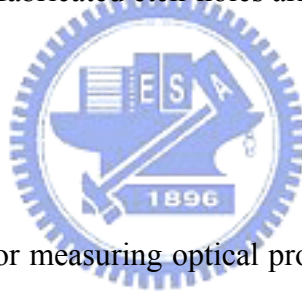
The configuration used for measuring optical properties of the microreflectors is depicted. The experimental setup is shown schematically in Fig. 5.1. A He-Ne laser (λ = 633 nm) is directed toward the perforated film after passing through a variable attenuator, a spatial filter, and a collimating lens to emerge as a collimated beam. The beam uniformly fills the entrance pupil of the telescope system and scale the diameter of beam size down to 200 μm. The sample is mounted on a plate riding on a translation stage. An etch-holes array acts as a 2D diffraction grating that diffracts the laser beam into several diffraction orders. The diffraction pattern is captured and analyzed by means of a CCD camera and a personal computer, respectively.
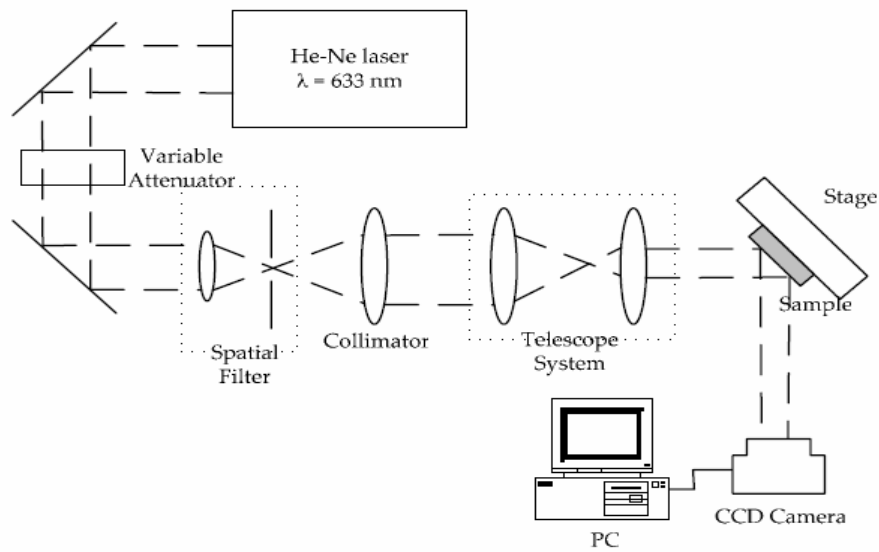
Fig. 5.1 The measurement systems

5.3 Fabrication Results

The fabrication results of the 45°-fixed micromirror shows in Fig. 5.3 (a)-(c). A micro polarization beam splitter (PBS) with single Si_3N_4 thin film is developed in the same self-assembly process, and shown in Fig. 5.2. Because of Babinet's principle, the diffraction fields reflected or transmitted from the PBS with etch-holes array have the same results, which are in agreement in the mocroreflector model we calculated before.
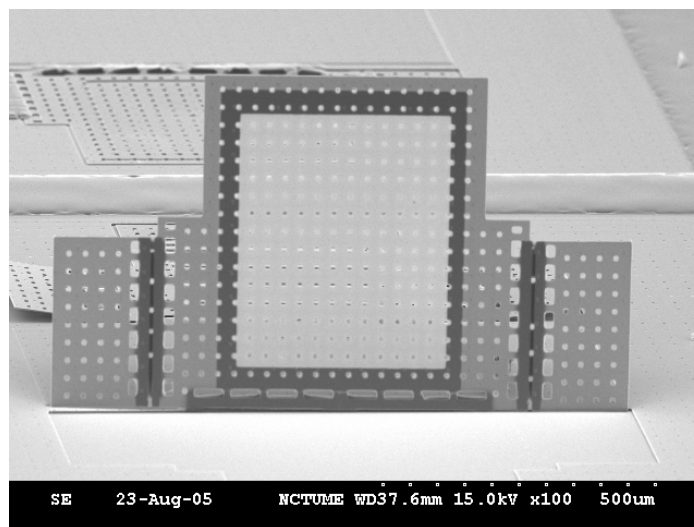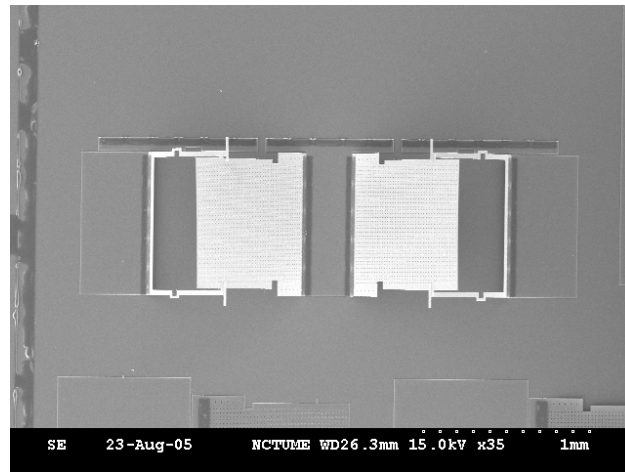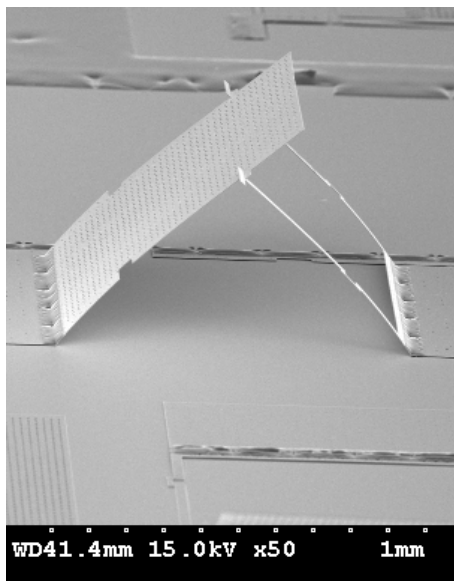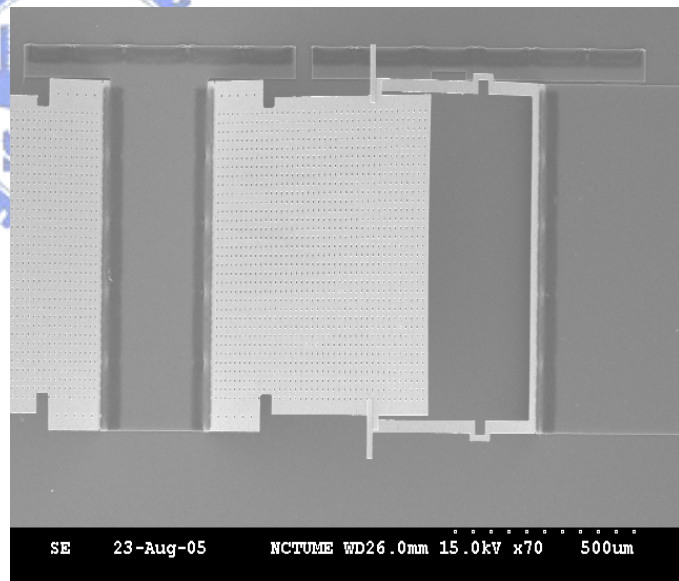

Fig. 5.2 A micro PBS with single Si_3N_4 thin film

(a)

(b)

(c)

Fig. 5.3 SEM photographs of (a) Top view of two micromirrors, (b) Side view
of a micromirror, and (c) Zoom in on a micromirror

5.4 Measurement Results

To verify the relationship between diffraction and etch-holes layout, we develop a 2D micromirror through MUMPS (Multi-User MEMS Processes). The micromirror contains various etch-holes layouts compatible with MUMPS deign rules. Since we aim to study the dependence of diffraction behavior on various etch-holes array, the MUMPS mirror is not released from the substrate.

The measured irradiance distributions of various etch-holes features are shown. Fig. 5.4 shows the measured diffraction image of etch-holes array with regular spacing. Fig. 5.5 (a) (b) show the images compared with the calculated results for the array in random transition and additional rotation with random angles, respectively. The measured results make a close agreement with the previous simulation and qualitatively confirm our theoretical analysis based on Fraunhofer diffraction theory.
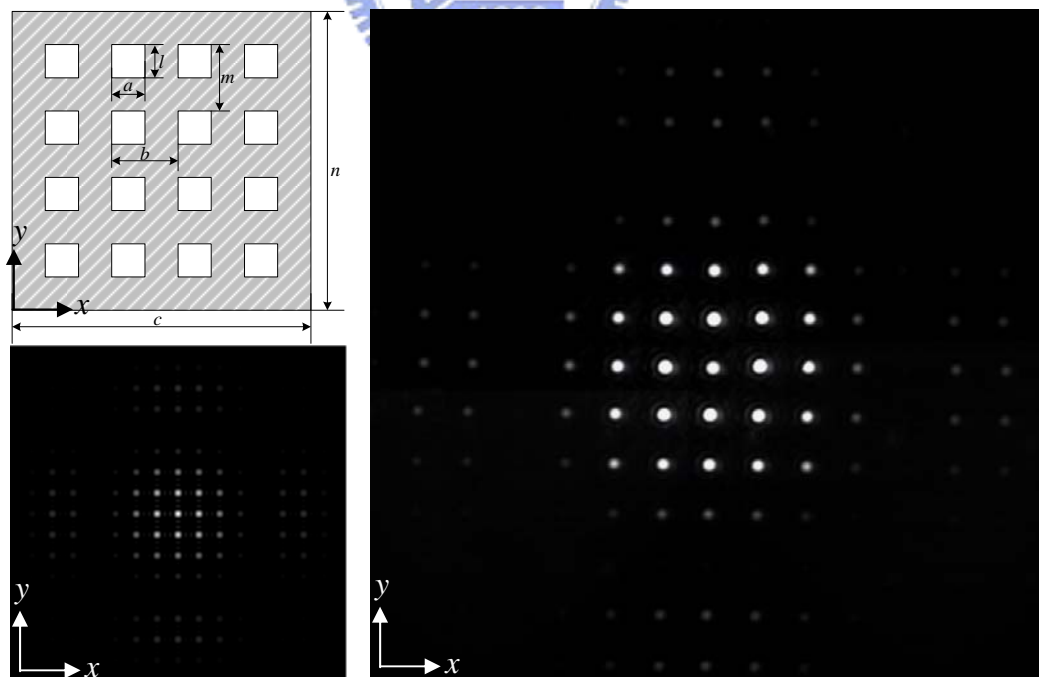

Fig. 5.4 The measured image of etch-holes array with regular
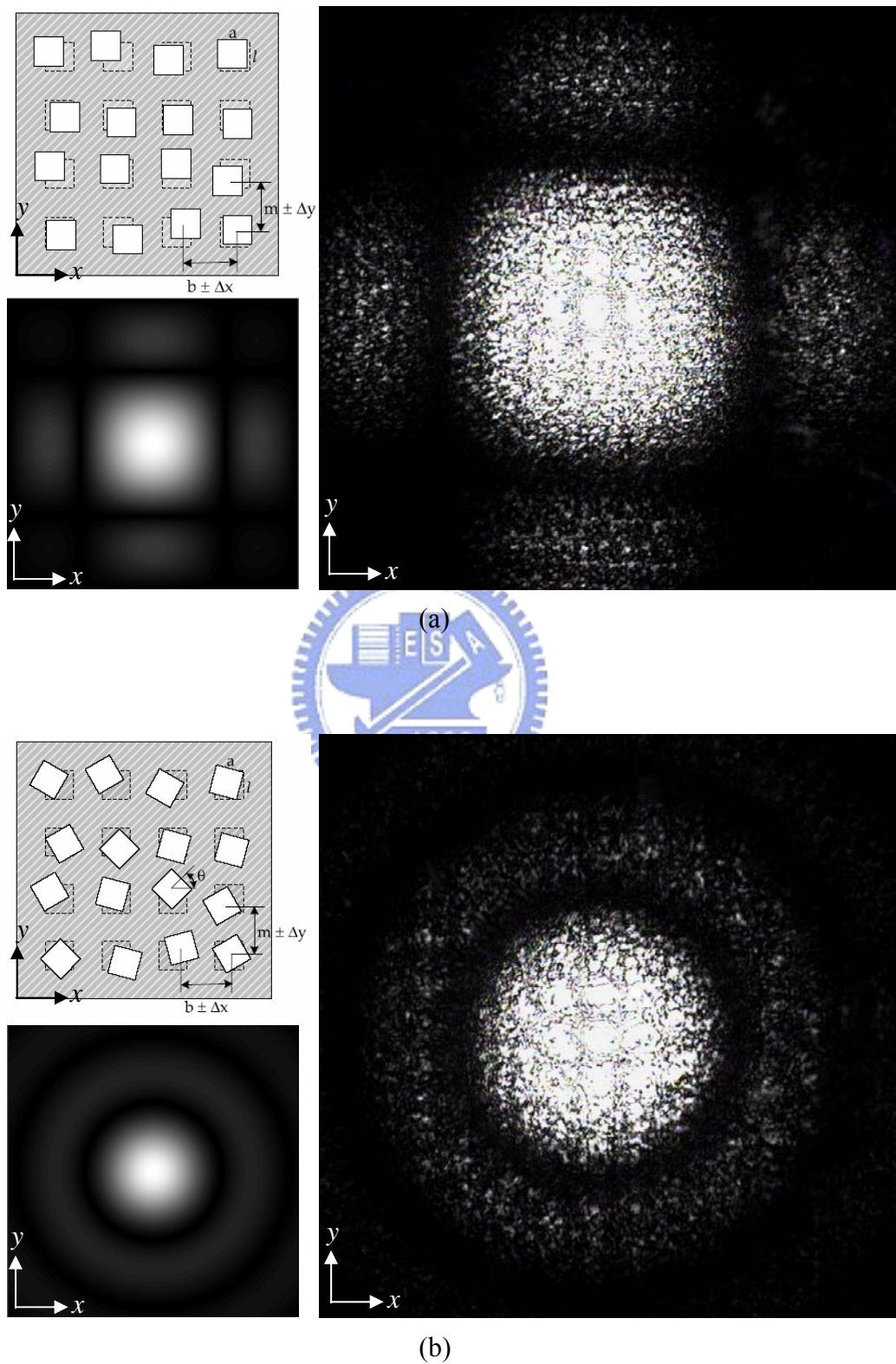spacing compared with its calculated result

(a)

(b)

Fig. 5.5 The images compared with their calculated results for(a) the array in
random transition and (b) additional rotation with random angles.

Because of the reactive ion etching (RIE), the form of the square hole in geometry is close to octangle. Fig. 5.6 shows the close-up of the etch holes. Such octangle holes cause the envelope of the diffraction pattern in Fig. 5.4 looks close to octangle in geometry. Besides, the dimples by the side of etch holes in Fig. 5.6 are necessary in our MUMPs-like process. They cause some phase shifts of the wavefront, but they are too shallow to cause no effects. In this thesis, we ignore the effects caused by dimples.
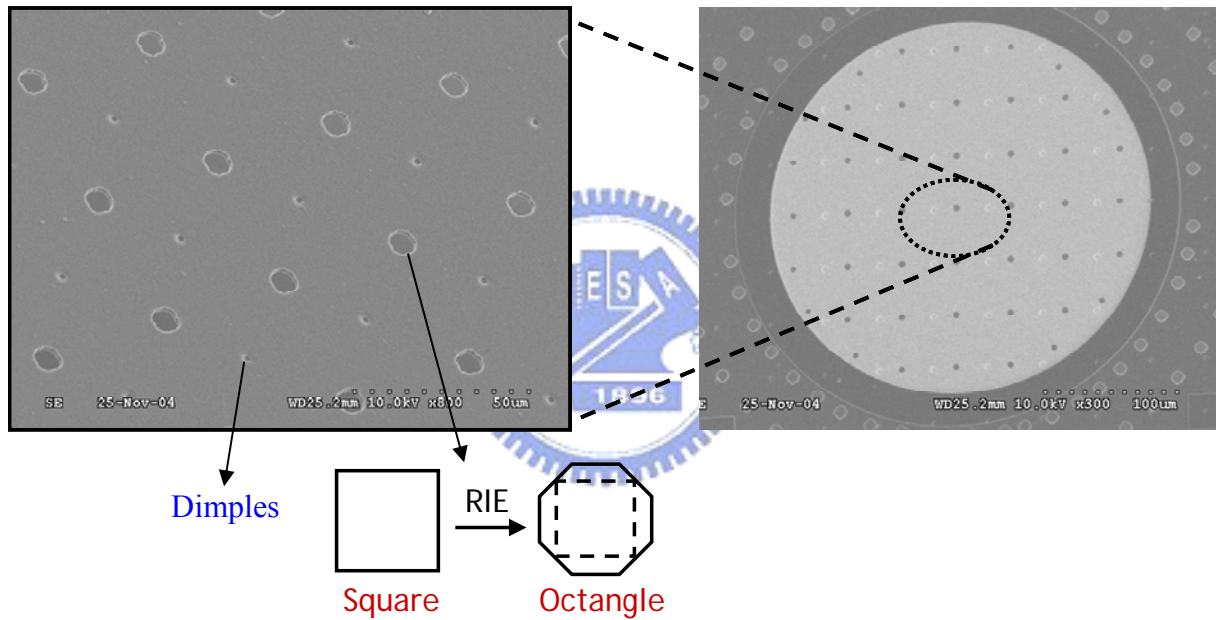
Fig. 5.6 the close-up of the etch holes on a devices

Fig. 5.7 shows the measured results of the concentric array. The high diffraction beams can be certainly reduced. The concentric layouts can be used as a beam shaper for centralizing the beam.

Fig. 5.7 The images of the two cases used the concentric
array compared with the regular case.

5.5 Summary

The self-assembly devices, microreflector and micro PBS, are demonstrated. The microreflectors with different etch-holes layouts are measured to verify the calculated results. In fact, the measured results show the fabricated etch-holes array match our purpose.

Chapter 6

Conclusions

6.1 Optical Analyses

To summarize, optical MEMS typically require etch holes to reduce the time required to release the micromechanical structure during the sacrificial unde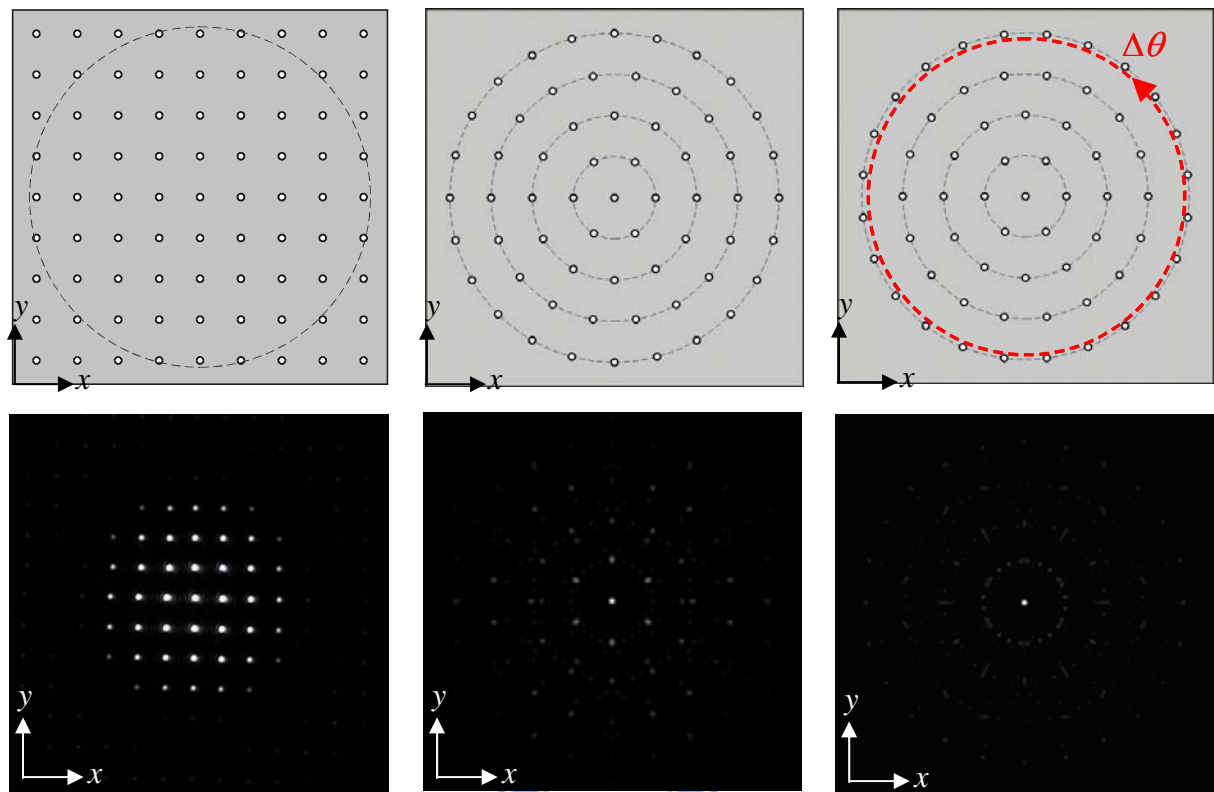rcutting. However, the size and density of the etch-holes array has a strong effect on the diffraction patterns, which plays a key role in most optical characteristics. In this thesis, we examined the dependence of diffracted pattern on the etch-holes configuration based on an analytical Fourier study. The diffracted irradiance caused by etch-holes array is contributed by two factors, namely, array factor and shape factor. Array factor determined by the period of the etch holes can cause high-order diffraction beams, which can be averaged out by use of random translation layout. On the other hand, the shape factor determined by the form factor of each element provides the envelope of the overall diffraction pattern. The envelope can be centrally symmetrized by the randomly rotation of each element. These diffraction fields are similar to the light through single circle and square aperture. The analysis is suitable on all transmission or reflection plate-type micromachined devices.

Otherwise, concentric etch-holes array has been proposed without varying the arrangement density and the well-etching interval between holes. The diffracted high order beams are reduced by destructive interference between 0th and m-th ring. The diffraction efficiency is at least 50% compared with 80% in traditional case. Moreover, the diffraction efficiency can be reduced as 18% by rotated the 4th ring with $\theta_4/2$. To

summarize the analyses, Table-6.1 lists the optical qualities of several etch-holes layouts.

Table 6.1 the compare of different etch-holes arrangement

Arrangement Type	Impulse Response	Diffraction Efficiency $E = I_{max} / I_0$	Characteristic
Regular Distribution	$h(x) = sinc(af_x)\left[\sum_{k_x=-\infty}^{\infty} sinc(c(f_x - \frac{k_x}{b}))\right]$	>80%	Field is formed by *sinc* functions with *sinc*-type envelope.
Random Distribution	$h(x) = sinc(af_x)\left[1 + e^{-j2\pi b_1 f_x} + e^{-j2\pi b_2 f_x} + \ldots\ldots\right]$	Uniform Field	High order diffraction beams are averaged out.
Circular Distribution	$h(x,y) = \frac{a}{\rho} J_1(2\pi a\rho)$ $\times \sum_{m=0}^{M}\sum_{n=0}^{N_m}\exp\left[-j2\pi r_m(f_x\cos n\theta_m + f_y\sin n\theta_m)\right]$	18%~50%	High order diffraction beams are reduced by destructive interference.

6.2 Micro Fabrication

In experiment, we successfully produced the devices, microreflectors and micro PBS, with designed etch-holes layouts to verify the calculation results by self-assembly technology. Fig. 6.1 shows the pictures of three kinds of etch-holes layouts captured from the devices. Optical experiments quantitatively confirmed our analyses. The proposed design of random distributed etch-holes array is expected to provide a useful consideration for future surface micromachining design rule.
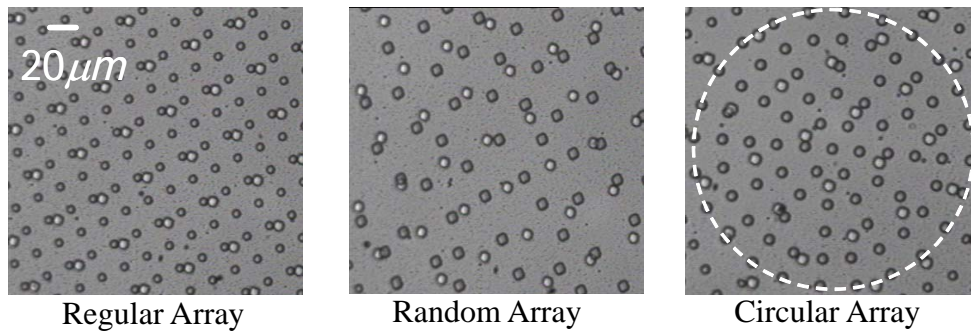
<div align="center">Regular Array   Random Array   Circular Array</div>

Fig. 6.1 Pictures of three kinds of etch-holes layouts captured from the devices

6.3 Future Works

According to our experimental results, the optical properties of the micro devices produced by the self-assembly technology are analyzed. However, the discussions in the thesis are all analyzed by Fraunhofer approximation. There are many interesting effects, e.g. Telbot effect, in the Fresnel region. Therefore, the diffraction caused by etch-holes array in Fresnel approximation will be discussed. Moreover, we will combine the self-assembly devices with movable mechanisms. For example, an adjustable polarization beam splitter with micro actuator will be demonstrated.

Reference

[1] Peter F. Van Kessel, Larry J. Hornbeck, Robert E. Meier, and Michael R. Douglass, "A MEMS-Based Projection Display," *Proceedings of the IEEE*, vol. 86, no. 8, August 1998.

[2] Paul M. Hagelin, Student, and Olav Solgaard, "Optical Raster-Scanning Displays Based on Surface-Micromachined Polysilicon Mirrors," *IEEE Journal of Selected Topics in Quantum Electronics,* vol. 5, no. 1, January/February 1999.

[3] R. Apte, F. Sandejas, W. Banyai and D. Bloom, *" Grating Light Valves for High Resolution Displays,"Solid State Sensors and Actuators Workshop*, June 1994.

[4] M. C. Wu, L. Y. Lin, S. S. Lee, and K. S. J. Pister, "Micromachined free-space integrated micro-optics," *Sens. Actuators: A (Physical)*, Vol. 50, pp. 127-134, 1995.

[5] R. T. Howe and R. S. Muller, "Polycrystalline silicon micromechanical beams," *J. Electrochem. Soc.*, Vol. 130, pp. 1420–1423, 1983.

[6] MEMS Technology Applications Center, Microelectronics Center at North Carolina (MCNC), Research Triangle Park, NC, and Integrated Micro Electro Mechanical Systems, offered at Analog Devices, Cambridge, MA.

[7] D. Koester, A. Cowen, R. Mahadevan, and B. Hardy, *PolyMUMPs Design Handbook Revision 10.0*.

[8] W. N. Sharpe, Jr., R. Vaidyanathan, B. Yuan, G. Bao and R. L. Edwards, "Effect of etch holes on the mechanical properties of polysilicon," *J. Vac. Sci. Technol.* Vol. B 15, pp. 1599-1603, 1997.

[9] X. Fang, N. Myung, K. Nobe, and J. W. Judy, "Modeling the effect of etch holes on Ferromagnetic MEMS," *IEEE Tran. on Magnet*. Vol. 37, pp. 2637-2639,

2001.

[10] J. Zou, M. Balberg, C. Byrne, C. Liu, and D. J. Brady, *"Optical properties of surface micromachined mirrors with etch holes," IEEE J. Microelectromech. Syst.*, Vol. 8, pp. 506-513, 1999.

[11] J. W. Goodman, *Introduction to Fourier Optics* (McGraw-Hill, Singapore), pp. 35-36.

[12] Eugene Hecht, *Optics* (Addison Wesley, San Francisco), pp. 508-509.

[13] K. Iizuka, *Elements of Photonics* (Wiley-Interscience, New York, USA), pp. 32-40.

[14] W. H. Beyer, *CRC Standard Mathematical Tables, 28th ed.*, (CRC Press, FL., 1987).

[15] J. A. Walraven, "Failure mechanisms in MEMS," *IEEE ITC International Test Conference* Paper 33.1, pp. 828-833, 2003.